Hepatic lipid-associated macrophages mediate the protective effects of bariatric surgery against NASH

Gavin Fredrickson[1], Kira Florczak[1], Fanta Barrow[1], Katrina Dietsche[1], Preethy Parthiban[1], Rawan Almutlaq[1], Maya Abujamra[1], Maya Demirchian[1], Haiguang Wang[1], Huy Nguyen[1], Oyedele Adeyi[2], Alessandro Bartolomucci[1], Christopher Staley[3], Cyrus Jahansouz[3], Jesse Williams[1,4], Douglas G. Mashek[5], Sayeed Ikramuddin[3*], and Xavier S. Revelo[1,4,6*]

[1]Department of Integrative Biology & Physiology, University of Minnesota, Minneapolis, MN 55455, USA.
[2]Department of Laboratory Medicine and Pathology, University of Minnesota, Minneapolis, MN 55455, USA.
[3]Department of Surgery, University of Minnesota, Minneapolis, MN 55455, USA.
[4]Center for Immunology, University of Minnesota, Minneapolis, MN 55455, USA.
[5]Department of Biochemistry, Molecular Biology, and Biophysics, University of Minnesota, Minneapolis, MN 55455, USA.
[6]Lead contact
*Correspondence: xrevelo@umn.edu or ikram001@umn.edu

Contact Information
Xavier S. Revelo, Ph.D.
Cancer and Cardiovascular Research Building
2231 6th St SE
Minneapolis, MN 55455
Phone: +1 (612) 301-7688

SUMMARY

Immune mechanisms are considered a major contributing factor to the inflammatory process and progression of non-alcoholic steatohepatitis (NASH). Bariatric procedures such as vertical sleeve gastrectomy (VSG) have been shown successful in ameliorating the progression of the disease. Several mechanisms of weight-loss-independent improvements due to bariatric surgery have been proposed including bile acid signaling, gut hormones, intestinal tissue reprogramming, and changes in the gut microbiome. However, whether bariatric surgery ameliorates the progression of NASH through anti-inflammatory mechanisms has not been investigated. To determine the effects of VSG on hepatic inflammation, we fed mice a high-fat high-carbohydrate (HFHC) diet for 12 weeks and assigned them to either VSG or Sham surgeries. Independent from weight loss, VSG resulted in reduced hepatic lipid accumulation and ameliorated NASH as early as 5 weeks after VSG. To profile the gene expression of macrophages in the NASH liver following VSG, we performed single-cell RNA sequencing and identified 18 clusters of monocytes and macrophages with a unique gene expression signature. We found substantial alterations in macrophage subsets in association with VSG-induced reversal of NASH. In particular, hepatic lipid-associated macrophages (LAMs), which are enriched in genes associated with lipid metabolism and collagen degradation, were highly responsive to VSG. Differential gene expression analysis revealed that VSG increased the expression of genes involved in lysosomal activity, antigen presentation, and repression of inflammation in LAMs, suggesting that VSG sustains their protective function. Spatial transcriptomic analysis of human liver sections confirmed the enrichment of LAM genes within periportal regions during NASH and a marked reduction following VSG. To determine a causal role for hepatic LAMs in the restorative process induced by VSG against NASH, we performed VSG in mice deficient for the triggering receptor expressed on myeloid cells 2 (Trem2). TREM2-deficiency ablated the protective effects of VSG against NASH, suggesting that LAMs mediate this reparative process. Mechanistically, Trem2 prevents the inflammatory activation of bone marrow-derived macrophages, in agreement with the anti-inflammatory effects of VSG in LAMs. Overall, our findings suggest that bariatric surgery improves NASH through a reparative process driven by hepatic lipid-associated macrophages.

INTRODUCTION

Non-alcoholic fatty liver disease (NAFLD) is estimated to affect 30% of the population and is one of the leading causes of abnormal liver function[1]. Fatty liver disease is highly associated with obesity and covers a wide spectrum of liver pathology ranging from a simple lipid accumulation to the more serious non-alcoholic steatohepatitis (NASH), characterized by inflammation, hepatocellular injury, and fibrosis[2, 3]. Hepatic inflammation is primarily driven by liver macrophages and is a critical component in the initiation and progression of NASH[3, 4]. Although lifestyle and dietary intervention can result in moderate weight loss with concomitant improvements in comorbidities, these effects are invariably transient and weight regain is common[5]. Bariatric procedures such as vertical sleeve gastrectomy (VSG) are the most successful and effective treatment options for obese adults[6] and are successful at ameliorating the progression of NASH[7-9]. While changes in body weight have a profound metabolic impact, bariatric surgery often results in improved insulin sensitivity before any substantial weight loss, suggesting weight-loss-independent effects[10, 11]. Several mechanisms of weight-loss-independent improvements in metabolism due to bariatric surgery have been proposed including bile acid signaling[12], gut hormones[13], intestinal tissue reprogramming[14], and changes in the gut microbiome[15, 16]. However, whether bariatric surgery ameliorates the progression of this disease through anti-inflammatory mechanisms has not been investigated.

Recent research has shown that NASH is associated with the emergence of macrophages with a lipid-associated signature, including the triggering receptor expressed on myeloid cells-2 (Trem2)[17, 18]. These macrophages have been termed hepatic lipid-associated macrophages (LAMs)[17], are conserved in mice and humans, correlate with disease severity, and are highly responsive to dietary intervention[18]. In NAFLD, LAMs are induced by lipid exposure and preferentially localize to steatotic regions[19]. TREM2 is needed for adequate metabolic coordination between macrophages and hepatocytes, lipid handling, efferocytosis, and extracellular matrix remodeling[20-22]. As a result, TREM2 deficiency aggravates NAFLD progression and its susceptibility to sepsis[21]. In a mouse model of hepatotoxic injury, TREM2 deficiency in non-parenchymal cells prevented inflammation-associated injury by interfering with toll-like receptor signaling[23]. As TREM2 has emerged as a central signaling hub regulating macrophage function, targeting the TREM2 pathway is the focus of several therapeutic efforts. Most notably, antibodies and molecules that either stimulate the TREM2 active domain or block its shedding are being tested in neurogenerative diseases[24]. However, despite the evidence suggesting that LAMs are protective against NASH, the mechanisms underlying their restorative function in NASH are unknown.

In the current study, we found that VSG ameliorates the progression of NASH and results in substantial alterations in macrophage subsets in association with disease reversal, independent from weight loss. Most notably, the newly described hepatic lipid-associated macrophages (LAMs)[17], whose counterparts maintain lipid homeostasis in adipose tissue[25], were highly responsive to the surgery. Indeed, TREM2-deficiency prevented VSG from exerting its protection against NASH, suggesting that LAMs are required by this reparative process. In vitro, Trem2 prevents the inflammatory activation of bone marrow-derived macrophages, highlighting the anti-inflammatory role of LAMs in response to VSG. Overall, our results show that bariatric surgery improves NASH through a reparative process driven by hepatic lipid-associated macrophages.

RESULTS

Vertical sleeve gastrectomy ameliorates NASH progression independent of weight-loss

We used a validated mouse model of VSG in which approximately 80% of the lateral stomach of mice is excised and a gastric clip is placed[15]. To induce NASH, we fed mice a high-fat high-

carbohydrate (HFHC) diet that recapitulates aspects of human disease such as obesity, hepatic lipid accumulation, inflammation, and fibrosis[26]. Mice were fed the HFHC diet ad libitum for 12 weeks and then assigned to either sham (Sham AL) or VSG surgery (**Fig. 1A**) and remained on the HFHC diet for 5 weeks. Most mice survived the surgery, and we confirmed surgical anatomy by oral gavage of barium and imaging[15]. To determine weight-loss-independent effects, we included a sham group that was pair-fed to the VSG group (Sham PF) to match their weight loss during the post-surgery period[27]. In addition, a group of mice were fed a normal chow diet (**NCD**) for the duration of the studies. Compared with Sham AL mice, both VSG and Sham PF mice showed a similar decrease in average daily food intake (**Fig. 1B**), body (**Fig. 1C**), and liver weight (**Fig. 1D**). However, the VSG group showed improved steatosis (**Fig. 1E and 1F)**, NAS score (**Fig. 1G**), and ALT/AST (**Fig. 1H**) compared with Sham PF mice, suggesting that caloric restriction was not responsible for all the effects of VSG. Notably, the amount of excreted fecal lipids was increased in VSG relative to Sham AL mice (**Fig. 1I**), suggesting that decreased intestinal lipid absorption contributes to the VSG-induced improvements in NASH in a weight-loss-independent manner[12]. Additionally, we assessed the mice 10 weeks post-surgery. There was no difference in weight loss (**Fig. S1A**), liver weight (**Fig. S1B**), and serum AST (**Fig. S1C**) between the VSG and the sham groups. However, the VSG group maintained the improvements in ALT (**Fig. S1D**) and steatosis (**Fig. S1E**).

To determine if the VSG-induced improvements in NASH were associated with restored gut microbiota and its metabolites, we analyzed the fecal microbial composition in NCD, Sham AL, Sham PF, and VSG mice. Compared with NCD mice, HFHC feeding induced dramatic remodeling in gut microbial species, including increased abundances of Akkermansia, Erysipelotrichaceae, Parasutterella, Ruminococceae, Clostridium XVIII, and decreased abundances of Lactobacillus, and Alistipes (**Fig. 1J and File S1**). While no differences were detected between all HFHC-fed mice at baseline, VSG resulted in a substantial decrease in Clostridium XVIII (**Fig. 1K**) and a restoration of Lactobacillus towards levels found in NCD mice (**Fig. 1L**). There were no significant differences in fecal microbiota composition between Sham AL and Sham PF mice (**File S1**). Because intestinal products can translocate into the portal vein and reach the liver, we then measured the concentrations of bile acids (BA) and short-chain fatty acids (SCFA) in the portal vein blood. While HFHC feeding increased the total amount of BA in Sham AL mice, both Sham PF and VSG decreased BA concentrations to levels similar to NCD mice (**Fig. 1M**). In particular, VSG and Sham PF lead to a similar decrease in taurine-conjugated cholic acid (TCA) while VSG was more effective at reducing DCA and TDCA than Sham PF (**Fig. 1N**). Independent of surgical intervention, HFHC feeding decreased the levels of CA, CDCA, and HDCA and increased several taurine-conjugated BA without any effects of VSG (**Fig S1F**). HFHC feeding also decreased the concentration of SCFAs in hepatic portal serum and neither VSG nor Sham PF had an impact on the concentration (**Fig. 1O and File S2**). These data suggest that the weight-loss-independent VSG improvements in NASH are associated with a partial restoration of specific gut microbial species and BAs.

Single-cell RNA sequencing shows that VSG exerts anti-inflammatory effects on LAMs

To profile the gene expression of macrophages in the NASH liver following VSG, we performed droplet-based scRNA-seq of magnetically sorted leukocytes from the livers of sham AL, sham PF, and VSG mice at 5 and 10 weeks after surgery (n = 4 mice per group/timepoint, **Fig. 2A**). Livers were perfused before immune cell purification to remove circulatory cells[28]. Prior to processing, we multiplexed samples using cell multiplexing oligos (CMOs) to track the sample of origin. Cells were loaded into the ports of a 10x-Genomics chip following a single-cell 3' kit. The gene expression and CMOs libraries were sequenced using a Novaseq S4 chip (2x150bp PE). After quality control, data were normalized and de-multiplexed. Monocytes and macrophages were

identified using the cell ID function of Seurat and re-clustered for analysis. We profiled the gene expression of approximately 39,033 (5 weeks) and 19,871 (10 weeks) single cells (avg. read depth 50,000). Unsupervised graph-based clustering was performed on the integrated dataset and cells were visualized using uniform manifold approximation and projection (UMAP). UMAP analysis revealed 8 major (18 total) clusters of monocytes and macrophages, whose identity was determined based on the expression of established marker genes[17] (**Fig. 2B and C**). Among the major clusters, we identified Kupffer cells (KC), Trem2^{+} LAMs, two clusters of monocyte-derived recruited macrophages (Mac1/2), as well as 4 clusters of classical (Mon1), patrolling (Mon3/4), and transitioning monocytes (Mon2, **Fig. 2B and C**). Although the origin (ontogeny) and cellular turnover of hepatic LAMs is unknown, recent work suggests that recruited monocyte-derived macrophages give rise to hepatic LAMs[20, 29]. To gain insight into the differentiation of macrophage subsets, we performed a slingshot trajectory analysis[30] of our integrated dataset. Using monocytes as the origin, we found two trajectories by which newly recruited monocytes differentiate into transitioning monocytes, MoMFs, LAMs, and either our Mac-1 or KC-1 clusters (**Fig. 2D and Fig. S2**). While the relative proportions of other macrophages remained similar at 5 weeks post VSG, we observed that VSG resulted in a marked effect on the Mac1 and LAM subset at 10 weeks post-VSG (**Fig. 2E**). Indeed, Trem2 expression decreased in VSG mice at week 10 post-VSG (**Fig. 2F**), suggesting that VSG reprograms their gene expression to exert an unknown biological effect independent from weight loss. To better understand how VSG alters the gene expression profiles of hepatic macrophages, we performed differential gene expression analysis between Sham AL, Sham PF, and VSG groups. First, we compared the gene expression of all macrophage clusters and identified distinct expression patterns in macrophages from Sham AL, Sham PF, and VSG mice at 5 and 10 weeks after surgeries (**Fig. S3**). Next, we focused on the effects of VSG on the expression of LAMs at 5 weeks after surgery to capture early effects on their gene expression. Compared with Sham AL and to a lesser extent Sham PF, LAMs from VSG mice showed increased expression of genes involved in lysosomal activity (Lyz2, *Ctsl, Ctss,* and *H2-Eb1*), antigen presentation (*H2-Eb1*), and repression of inflammation (*Egr1*) while downregulated several inflammatory genes (*Cd83*, *Nfkb1*, *Junb*, and *Mmp7*) at the 5-week post-VSG timepoint (**Fig. 3**). Thus, these data highlight several regulatory mechanisms by which VSG may sustain the protective function of LAMs during NASH reversal in response to VSG.

Spatial transcriptomic analysis of NASH livers following bariatric surgery

To assess the effects of VSG on human livers we performed spatial transcriptomics on specimens from a patient with NASH, and a different patient with NASH before and one year after VSG (**Fig. S4A**). VSG resulted in the resolution of NASH in this patient (NAS 4 to NAS 0 after 12 months). After staining with cytokeratin (green) and the macrophage marker CD68 (magenta), 32 regions of interest were annotated to define hepatic zones I, II, and III (**Fig. S4B**). Unsupervised PCA of detectable genes revealed a substantial separation between specimens but small differences between hepatic zones (**Fig. S4C**). Pathway analysis of differentially expressed genes in the Pre-VSG vs. Post-VSG comparison revealed a downregulation of pathways involved in the "metabolism of lipids", "cholesterol biosynthesis", and "metabolism of steroids" while "metabolism of aminoacids" was upregulated (**Fig. S4D and S4E**). To explore if human LAMs are responsive to VSG, we assessed the expression of genes involved in the LAM differentiation program such as *Trem2*, *Plin2*, *Ctss*, *Cd36*, and *Lipa*[29, 31]. LAM genes were primarily enriched in zone I of the liver in the NASH and Pre-VSG sample but were downregulated in the Post-VSG sample (**Fig. S4F**), suggesting that LAMs correlate with disease progression in human NASH.

Given that our scRNA seq analysis revealed substantial changes in the gene expression profile of hepatic macrophages, we next performed spatial transcriptomic analysis of liver sections (Nanostring GeoMx) to explore the effects of VSG on the hepatic areas surrounding the macrophages. Tissues from NCD, Sham AL, Sham PF, and VSG mice were collected 5 weeks

after surgery and stained with a fluorescently labeled antibody against the macrophage marker CD68 to capture gene expression changes in CD68$^-$ microanatomic areas (**Fig. 4A**). Following imaging and sequencing, the initial data was subjected to quality checks, filtering, and scaling, leading to a total of 7074 detectable genes and 32-36 ROIs per group (**Fig. 4B**) Unsupervised principal component analysis (PCA) of the normalized genes showed a substantial separation between CD68-expressing ROIs, and to a lesser extent between experimental groups (**Fig. 4C**). To determine how gene expression was altered in the CD68$^-$ ROIs, we performed differential gene analysis. We identified 187, 105, and 141 differentially expressed genes (DEGs: FDR<0.05, FC > 1.5) between NCD vs. Sham AL (**Fig. 4D**), Sham AL vs. and VSG (**Fig. 4E**), and Sham PF vs. VSG (**Fig. 4F**), respectively. Gene set enrichment analysis (GSEA) revealed that our analysis led to an overall substantial coverage in pathways such as “metabolism”, “immune system”, and “metabolism of proteins” (**Fig. S4G**). Compared with the NCD group, Sham AL downregulated genes involved in the “metabolism of steroids” and “respiratory electron transport” pathways and an upregulated of “plasma lipoprotein remodeling” and “chemokine receptors bind chemokines” (**Fig. 4G**). Compared with Sham AL, VSG downregulated pathways involved in “biological oxidations”, “metabolism of amino acids”, and “metabolism of lipids” in agreement with the reduced lipid accumulation observed in VSG mice. On the other hand, VSG upregulated pathways such as “degranulation of neutrophils/platelets” and “complement cascade” indicative of an active immune and tissue remodeling response (**Fig. 4H**). Compared with the Sham PF group, we observed a downregulation of metabolic pathways and an upregulation of complement pathways in the VSG ROIs, similar to the VSG-induced changes relative to the Sham AL group (**Fig. 4I**). Overall, these findings highlight the VSG-induced transcriptomic changes in the microenvironment surrounding hepatic macrophages that are associated with NASH reversal.

Hepatic Trem2$^+$ LAMs mediate the reparative effects of VSG against NASH

Recent work has shown that systemic TREM2 deficiency aggravates NASH as TREM2 is required for LAM survival, the metabolic coordination between LAMs and hepatocytes, and the clearance of dying liver cells[20-22, 31]. While it is becoming clear that LAMs are protective against NASH[31], the mechanisms by which they promote disease reversal are unknown. To determine if LAMs directly mediate the restorative process induced by VSG against NASH, we performed sham or VSG surgeries on WT and Trem2 KO mice fed a HFHC diet for 12 weeks. Five weeks post-surgery, WT and Trem2 KO mice showed a similar degree of weight loss (**Fig. 5A**) and an increase in fecal lipid excretion (**Fig. 5B**) in response to VSG. However, while VSG ameliorated NASH in WT mice, this effect was blunted in Trem2 KO mice (**Fig. 5C-G**). Specifically, VSG failed to decrease the liver weight (**Fig. 5C**), hepatic steatosis (**Fig. 5D and 5E**), ALT (**Fig. 5F**), and AST (**Fig. 5G**) in Trem2 KO mice, suggesting that Trem2 is required for the VSG-induced reversal of NASH. To explore the underlying mechanisms, we first assessed whether Trem2 deficiency alters hepatic macrophage populations at baseline during NASH (**Fig. S5A**). Compared with WT controls, HFHC-fed Trem2 KO mice showed no differences in body weight (**Fig. S5B**) and the number of macrophages populations including monocyte-derived macrophages (MoMF), F4/80^{hi} CD11b^{int} macrophages, VSIG4- macrophages, embryonic Kupffer cells (emKC), and monocyte-derived Kupffer cells (moKC, **Fig. S5C-I**), suggesting that Trem2 deficiency does not alter the number of additional hepatic macrophage populations in NASH.

To investigate the potential mechanisms by which Trem2 deficiency alters hepatic macrophages and prevents the protective effects of VSG against NASH, we magnetically isolated and performed bulk RNA sequencing on total macrophages from the liver of WT and Trem2 KO mice assigned to either Sham or VSG surgeries. Unsupervised PCA showed a clear separation between WT Sham and WT VSG, whereas there was no clear distinction between Trem2 KO Sham and Trem2 KO VSG macrophages (**Fig. S6A**). Differential gene expression analysis

revealed 779 DEGs for WT Sham vs. WT VSG, 132 DEGs for Trem2 KO Sham vs. Trem2 KO VSG, and 79 DEGs shared by both comparisons (**Fig. S6B**). Unsupervised clustering of the top 500 most variable genes revealed a substantial distinction between the gene expression profile of WT Sham and WT VSG macrophages (**Fig. S6C**). However, this difference in gene expression was not detected between Trem2 KO Sham and Trem2 KO VSG macrophages (**Fig. S6D**), suggesting that Trem2 is required for macrophages to respond to VSG. Furthermore, pathway analysis showed that WT VSG macrophages were enriched in genes associated with "cellular respiration' and "oxidative phosphorylation" and downregulated genes involved in "focal adhesion", compared with WT Sham controls (**Fig. S6E**). In contrast, Trem2 KO VSG macrophages were primarily enriched in genes involved in "ribosome"-related processes, relative to Trem2 KO Sham (**Fig. S6F**). Notably, we performed pathway analysis using the DEGs in the WT VSG vs. Trem2 KO VSG comparison to determine the differential effects of VSG in WT and Trem2 KO macrophages. WT VSG macrophages were enriched in "mRNA processing" and pathways related to metabolism such as "mitochondrion organization" and "oxidative phosphorylation" (**Fig. 6H**). Interestingly, Trem2 KO VSG macrophages were primarily enriched in inflammatory and immune-related pathways such as "inflammatory response" and "cytokine-cytokine receptor interaction" (**Fig. 6H**), suggesting that Trem2 prevents the inflammatory activation of macrophages in response to VSG. To test this possibility, we examined the responses of WT and Trem2 KO bone marrow-derived macrophages (BMDM) to an inflammatory stimulus. Compared with WT controls, Trem2 KO BMDMs showed a markedly increased expression of *Il1b*, *Il6*, and *Tnf* following palmitate activation (**Fig. 6I, top**) and in unstimulated conditions (**Fig. 6I, bottom**). Overall, these data suggest that Trem2-expressing LAMs mediate the VSG-induced reversal of NASH through anti-inflammatory effects on macrophages.

Bariatric surgery alters the lipid profile in hepatic macrophages

Our scRNAseq data shows that hepatic LAMs are uniquely equipped with the enzymatic machinery to recognize, scavenge, and catabolize lipids[19, 29]. To explore if LAMs can contribute to the restoration of local lipid homeostasis following VSG, we performed metabolic profiling of sorted LAMs from Sham AL and VSG mice 5 weeks after surgeries. Flow injection analysis-tandem mass spectrometry (FIA-MS/MS) and liquid chromatography-tandem mass spectrometry (LC-MS/MS, MxP® Quant 500 kit, Biocrates) of total hepatic macrophages revealed 317 unique detectable metabolites. The majority of the identified metabolites were lipid species, however, we also detected amino acids and bile acids (**Fig. 5A**). Unsupervised PCA of all detected metabolites showed a clustering of VSG samples and some separation from Sham AL specimens (**Fig. 5B**). Compared with Sham AL, VSG induced an increase in total phosphatidylcholines (PC) and sphingolipids (SM) in hepatic macrophages, but no changes in total triacylglycerols (TG), cholesterol esters (CE), fatty acids (FA), glycosylceramides (HexCer), ceramides (Cer), sphingolipids (SM), and diacylglycerols (DG, **Fig. 5C**). To further assess the effects of VSG on the lipid profile of hepatic macrophages, we assessed the composition of the major lipid species. VSG macrophages were enriched in monounsaturated fatty acid-PCs (MUFA-PC) and both (aa) and (ae) PCs (**Fig. 5D**). Additionally, VSG macrophages were enriched in SM-nonOHs and both long chain fatty acid-SMs (LCFA-SM) and very long chain fatty acid-SMs (VLCFA-SM) (**Fig. 5E**). There were no differences in the subspecies of FAs (**Fig. 5F**) and CEs (**Fig. 5G**). Relative to Sham AL, VSG macrophages had increased very long chain fatty acid-Cer (VLCFA-Cer) (**Fig. 5H**). Finally, we performed chain length enrichment of all lipid species and found that VSG macrophages were enriched in lipid species with a chain length of 36, 40, and 42; whereas Sham AL macrophages were enriched in chain lengths of 54 and 56 (**Fig. 5I**). Overall, these data indicate that macrophages respond to VSG by increasing their content of PCs, SMs, and long chain-length lipid species.

DISCUSSION

Bariatric surgeries are the most effective treatment options available for the treatment of obesity complications including NAFLD and NASH[7-9, 32]. Caloric intake is dramatically reduced after bariatric surgery and has been postulated as a primary mechanism of action[33, 34]. However, the amount of weight loss due to caloric restriction itself is surprisingly small[35]. This emphasizes the need to better understand the mechanisms by which VSG exerts its beneficial effects. Alterations in the gut microbiome[15], gut hormones[13], and reprogramming of intestinal glucose metabolism[14] have been proposed as mechanisms for mediating VSG. A recent study proposed that decreased intestinal bile acids and lipid absorption are additional weight-loss-independent mechanisms of VSG actions[36]. These findings are in accordance with our observed reduction in the concentration of BAs in the hepatic portal serum of VSG mice. However, while a previous report showed that whole-body FXR deficiency ablated the VSG-induced weight loss[12], the liver-specific BA receptor FXR was not implicated in mediating the effects of VSG[36]. Here, we show that VSG induces weight-loss-independent improvements in NASH pathogenesis mediated by Trem2^{+} lipid-associated macrophages, implicating immune responses and reduced inflammation as an important mechanism of VSG action. In support of this notion, systemic inflammatory mediators associated with obesity have been shown to gradually decline following bariatric surgery in human patients[37]. In mice, a previous study using bulk RNA sequencing of livers following VSG revealed that the top pathway enriched in VSG, relative to Sham PF livers, was 'innate immune response'[38]. Similarly, another study showed that VSG alters the composition of CD11c-expressing macrophages and increases the frequency of PMNs in the liver [39]. Overall, these data suggest that the innate immune system, not only is responsive to VSG, but mediates the protective effects of bariatric surgery against NASH.

Recent research has shown that NASH is associated with the emergence of LAMs[17], a novel population conserved in mice and humans and highly responsive to dietary intervention[18]. LAMs express a unique lipid-associated signature including TREM2, CD9, and osteopontin (OPN/SPP1)[17, 18, 40]. In NASH, LAMs are induced by lipid exposure and localize to steatotic and fibrotic regions[19, 31]. Notably, hepatic LAMs are needed for adequate metabolic coordination, lipid handling, extracellular matrix remodeling, and clearance of apoptotic hepatocytes[20-22, 31, 40]. However, metabolic stress and inflammation cause TREM2 shedding in LAMs resulting in the loss of immune homeostasis and aggravated disease[22]. During the progression of NASH, hepatocyte-derived sphingosine-1-phosphate upregulates the expression of Trem2 in infiltrating macrophages[22]. Although the exact mechanisms by which Trem2-expressing LAMs protect against NASH, several mechanisms have been proposed including efferocytosis of dying hepatocytes[22] and regulation of macrophage exosomes[21]. Using VSG as a model of NASH reversal, here we show that TREM2 has cell-intrinsic anti-inflammatory effects. However, future work is needed to reveal the molecular mechanisms by which TREM2 prevents inflammatory activation of macrophages in NASH.

In agreement with our findings, VSG causes a restoration of healthy gut microbiota[41, 42]. Increased Lactobacillus, considered a beneficial commensal bacteria[43, 44], has been proposed to be a mechanism by which VSG improves obesity and glucose tolerance[45]. As the potential ligands of TREM2 include bacterial products[46], it is possible that gut-derived microbial products have direct effects on LAMs. As macrophages recognize microbial antigens using their pattern recognition receptors (PPRs)[47], future work is needed to determine if PRRs (e.g. TLRs) play a role. In addition, changes in gut microbiota may influence hepatic macrophages via gut-derived metabolites drained via the portal vein[48]. For example, intestinal SCFA butyrate may be another mechanism by which VSG induces a reparative macrophage phenotype and improves NASH.

Although the origin (ontogeny) and cellular turnover of hepatic LAMs is unknown, recent work suggests that recruited MoMFs give rise to hepatic LAMs[20, 29]. Using monocytes as the origin, slingshot trajectory analysis[30] of the integrated dataset revealed two trajectories by which newly recruited monocytes during NASH differentiate into transitioning monocytes, MoMFs, LAMs, and either Mac-1 or KC-1 clusters. However, LAM-specific fate-mapping tools such as a genetic TREM2 reporter mouse are needed to corroborate this finding. Another limitation of our study is that we utilized a mouse with a systemic TREM2 deficiency. Although TREM2 is primarily expressed by myeloid cells, bacterial and viral infections have been reported to induce TREM2 expression in CD4 T cells[49, 50]. Additionally, TREM2-expressing macrophages in the adipose tissue have been shown to prevent obesity and adiposity, which could influence the development of hepatic steatosis[51]. While several key experiments such as our scRNAseq and spatial transcriptomics analyses show that hepatic LAMs are responsive to VSG, we cannot rule out the potential contribution of adipose tissue LAMs to the VSG-induced protective effects in the liver.

In summary, here we show that VSG induces a reversal NASH independent of weight loss accompanied by a substantial remodeling of the gut microbiota and hepatic macrophages. Notably, we report that hepatic TREM2$^+$ LAMs respond to VSG by increasing their expression of lysosomal and anti-inflammatory while downregulating inflammatory genes. Importantly, TREM2 deficiency ablates the protective effects of VSG, providing causal evidence that LAMs mediate the beneficial effects of bariatric surgery against NASH.

MATERIALS AND METHODS

Animals

Five-week-old C57BL/6J or TREM2 KO (027197) mice were purchased from The Jackson Laboratory and maintained in a pathogen-free, temperature-controlled environment. At six weeks of age, mice were fed a high-fat high-carbohydrate (HFHC, 40% kcal palm oil, 20% kcal fructose, and 2% cholesterol supplemented with 23.1 g/L d-fructose and 18.9 g/L d-glucose in the drinking water) diet ad-libitum for 12 weeks to induce NASH. Subsequently, they received either a sham operation or VSG surgery. Post-surgery, the mice are provided a liquid diet for 2 days and the HFHC diet was slowly introduced. 7 days post-surgery the mice were only fed the HFHC diet for the remainder of the study. To account for weight-loss-independent effects, there was a sham ad-libitum-fed group (Sham AL) and a sham group that was pair-fed (Sham PF) to the VSG group to match the weight loss post-surgery. Briefly, the amount of HFHC diet fed to the Sham PF group was the mean consumption of the VSG group from the preceding day. Additionally, there was a group of mice that were fed a normal chow diet (NCD) for the duration of the study. The Trem2 KO VSG studies only included the VSG and Sham AL group assignments. All animal experiments were approved by the University of Minnesota Institutional Animal Care and Use Committee.

Macrophage Characterization and Isolation

Intrahepatic immune cells were isolated from perfused livers using enzymatic digestion and density gradient centrifugation as previously described[52]. For flow cytometry, cells were incubated with fluorophore-conjugated primary antibodies for 30 mins at 4°C. Flow cytometry data were acquired on a Fortessa flow cytometer (BD Biosciences) and analyzed using Flowjo (TreeStar) software. For macrophage-specific assays, macrophages were isolated from immune cell suspensions using anti-F4/80 microbeads and a MACS separator (Miltenyi Biotech).

Bone marrow-derived macrophages

Bone marrow-derived macrophages (BMDM) were generated as previously described[53]. Briefly, bone marrow was isolated from femurs and tibias, then seeded in 2mL of conditioned media with

macrophage colony-stimulating factor (mCSF, 25ng/mL, BioLegend). 5 days later 1mL of conditioned media with mCSF (50ng/mL) was added. 7 days after seeding, the BMDMs were washed and stimulated with palmitate for 24 hours (200uM, Cayman Chemical). Total RNA was extracted from the BMDMs using the RNeasy Plus Mini kit (Qiagen). cDNA was prepared using the iScript cDNA Synthesis kit (Bio-Rad). Gene expression was calculated using the 2(-ΔΔCT) method and normalized to GAPDH.

Fecal lipid extraction

Fecal lipid extraction was performed as previously described[54]. Briefly, feces were collected, added to 5mL of PBS, and vortexed until the fecal pellets disintegrated. Following, 5mL of chloroform: methanol (2:1, v/v) was added and centrifuged at 1,000g for 10min. The lower liquid phase was collected, transferred to a glass tube, and evaporated in a fume hood. The remaining lipids were then weighed.

NASH Phenotyping

Hepatic triglycerides were assessed using a calorimetric assay (Cayman Chemical). Concentrations of serum ALT and AST were assessed by the University of Minnesota Veterinary Medical Center's Clinical Pathology Laboratory. Liver sections were fixed in 10% formalin and hematoxylin and eosin (H&E) staining was performed (Biorepository & Laboratory Services at the UMN Clinical and Translational Science Institute). Following, NAS scoring of the H&E-stained liver sections was performed by a blinded pathologist.

Macrophage metabolite sample preparation

Biocrates' commercially available MxP® Quant 500 kit enables the quantification of up to 630 metabolites from 26 compound classes (e.g. amino acids, biogenic amines, bile acids, fatty acids, phosphatidylcholines, ceramides, di- and triglycerides). Lipids and hexoses were measured by flow injection analysis-tandem mass spectrometry (FIA-MS/MS) and small molecules were measured by liquid chromatography-tandem mass spectrometry (LC-MS/MS). Briefly, a 56 well-based sample preparation device was used to quantitatively analyze the metabolite profile in hepatic macrophages. This device consists of inserts that have been impregnated with internal standards, along with a predefined sample amount. Subsequently, a phenyl isothiocyanate solution was added to derivatize some of the analytes (e.g. amino acids). After the derivatization was completed, the target analytes were extracted with an organic solvent, followed by a dilution step. The obtained extracts were then analyzed by FIA-MS/MS and LC-MS/MS methods using multiple reaction monitoring (MRM) for the detection of analytes.

Macrophage metabolite FIA-MS/MS and LC-MS/MS Acquisition

Biocrates' LC-MS/MS analysis was carried out using a Shimadzu LC-20AD XR (Shimadzu USA Manufacturing Inc Canby, Oregon) coupled to a Sciex QTRAP 5500 mass spectrometer (Sciex, Framingham, MA). Chromatographic separation was achieved using the Biocrates' C18 separation column (4.5x 100mm, 1.7uM) maintained at 50 °C. Mobile phases consisted of: A (0.2% formic acid in water) and B (0.2% formic acid in 95% acetonitrile). For the positive ion mode, flow rates were set at 0.8 mL/min, with an injection volume of 5uL. The flow rate of 0.8 mL/min was maintained from 0-4.70s, with a subsequent increase to 1.0 mL/min from 4.70-5.10 min. The flow rate was decreased back down to the initial rate (0.8 mL/min) for the remainder of the positive ion run time, 5.10-5.80min. The elution began with isocratic hold 100% A, 0-1.50min; 1.50-2.70min linear gradient 88-82.5% A; 2.70-4.00min linear gradient 82.5-50% A; 4.00-4.50min linear gradient 50-0% A; 4.50-5.00min, isocratic 0% A; 5.00-5.10min linear gradient 0-100% A; 5.10-5.80min, isocratic 100% A. For the negative ion mode, flow rates were set at 0.8 mL/min, with an injection volume of 5uL. The flow rate followed the same transitions as that of the positive ion mode. To restate, the flow rate of 0.8mL/min was maintained from 0-4.70min, with a subsequent

increase to 1.0 mL/min from 4.70-5.10, followed by a decrease to the initial flow rate (0.8mL/min) for the remainder of the negative ion run time, 5.10-5.80min. The elution started with isocratic 100% A, 0-0.50min; 0.50-2.00min linear gradient 75-50% A; 2.00-3.00min linear gradient 50-25% A; 3.00-3.50min linear gradient 25-0%; 3.50-5.10min isocratic hold 0% A; 5.10-5.80min isocratic hold 100% A. For the FIA, flow rates were set at 0.03 mL/min, with an injection volume of 5 uL. The flow rate of 0.03 mL/min was maintained from 0-2.4min, with a subsequent increase in flow rate to 0.20 mL/min for 2.4-3.0 and returned to the initial flow rate of 0.03 mL/min at 3.0min. The elution maintained an isocratic hold of 100% B for the entirety of the FIA run time, 0-3.0min.

Concentrations for all metabolites were calculated in the Biocrates MetIDQ™ software following the recommended analysis procedures (Biocrates Life Sciences AG, Innsbruck, Austria). The processed results were exported to tabular format and statistical analyses were performed using in-house software. Metabolites missing greater than 20% of measurements were excluded from the statistical analysis. Missing values were imputed using the k-nearest neighbors approach as implemented in the *impute* R-package[55]. Hypothesis testing was performed using a one-way ANOVA followed by a Tukey Honest Significant Difference posthoc test. The obtained p-values were corrected for multiple testing using a Benjamini and Hochberg adjustment. Lipid set enrichment was performed using LipidSuite software[56].

Serum bile acid sample preparation

100uL of hepatic portal vein serum and 20uL of the internal standard were added to a 2 mL centrifuge tube and mixed. 30ul of HCL (1M) and 1mL of acetonitrile were added to samples, mixed thoroughly for 1min, and centrifuges at 14,000g for 15min. 1mL of supernatant was transferred to a new tube and the solvent was removed using a vacuum concentrator. Samples were then reconstituted in 100uL (3/7; v/v) methanol/water. Following, they were placed into an ultrasonic bath for 10 and then centrifuged at 14,000g for 15min. The supernatant was transferred into an autosampler vial with a 300uL glass vial. The samples were then analyzed via an LC-MS/MS method utilizing MRM for analyte detection.

Serum bile acid LC-MS/MS Acquisition

Bile acids were acquired using an Agilent 1290 series HPLC (Agilent, Santa Clara, CA) with an Acquity C18 BEH (2.1mm x 50mm, 1.7 um) column coupled to an Agilent 6495C Triple Quadrupole (Agilent, Santa Clara, CA) mass spectrometer in negative ion-mode. The acquisition was performed as previously described [57]. Briefly, mobile phases of water and methanol containing ammonium acetate and ammonium hydroxide were used as A and B phases, respectively. The following gradient is used: 80% A for 0.05min, a stepwise linear decrease to 53% A at 0.1min, to 49% A at 2.0min, and to 28% A at 4.5min. The flow rate was set to 0.5 mL/min. A column wash at 100% B for 0.5min and re-equilibration at 100% A for 0.6min were performed at a flow rate of 0.8 mL/min. Dwell times were set to 20ms and both Q1 and Q3 were operated at unit resolution in MRM mode. Concentrations of samples were obtained using the appropriate mass spectrometry software. The acquired data was imported into Agilent MassHunter software for additional analysis.

Serum short-chain fatty acid sample preparation

90uL of hepatic portal vein serum and 10uL of the internal standard were added to a 2mL centrifuge tube and mixed. Subsequently, 420uL of cold methanol was added to the samples. Samples were then vortexed for ~10 seconds, incubated for 10min at -20°C, and centrifuged for 10min at 14,000 g. 40uL of each sample was transferred to a new 2mL centrifuge tube. Following this, 20uL of the 3NPH and 20uL of the EDC solution were added to the samples and then incubated at 40°C for 30min. 1520uL (20:1, solvent:sample) water/ACN (9/1; v/v) was added for the sample dilution. Following the dilution step, 100uL of the diluted sample was transferred to an

autosampler vial with a 300uL glass insert. The samples were then analyzed via an LC-MS/MS method utilizing MRM for analyte detection.

Serum short-chain fatty acid LC-MS/MS acquisition

Short-chain fatty acids were acquired using an Agilent 1290 series HPLC (Agilent, Santa Clara, CA) with an Acquity C18 BEH (2.1mm x 50mm, 1.7 um) column coupled to an Agilent 6495C Triple Quadrupole (Agilent, Santa Clara, CA) mass spectrometer in negative ion-mode. Mobile phases of separation consisted of A-methanol/2-propanol (1/1; v/v) and B- methanol/water (1/1; v/v). Negative ion mode was utilized for acquisition, with an injection volume of 10 uL. Flow rates began at 0.5 mL/min for 0-4 min, with a subsequent decrease in rate to 0.25 mL/min for 4-12min, before returning to the initial flow rate of 0.5 mL/min for the remainder of the run time, 12-25min. The elution began with a linear gradient of 95-55% A, 0-4min; 4-12min linear gradient of 55-52.5% A; 12-15min linear gradient of 52.5-2% A; 15-17min isocratic hold 2% A; 17-17.1 min linear gradient 2-95% A; 17.1-25min isocratic hold 95% A. Concentrations of samples were obtained using the appropriate mass spectrometry software. The acquired data was imported into Agilent MassHunter software for additional analysis.

Bulk RNA Sequencing

Total RNA was extracted from hepatic macrophages using the RNeasy Plus Mini kit (Qiagen). Samples were sequenced on a Novaseq 6000 using a 150 PE flow cell at the University of Minnesota Genomics Center. The SMARTer Stranded RNA Pico Mammalian V2 kit (Takara Bio) was used to create Illumina sequencing libraries. Differential gene expression analysis was performed using edgeR (Bioconductor). Gene ontology and pathway analysis were completed using iDEP.96 software[58].

Fecal DNA extraction and sequencing

DNA was extracted from single fecal pellets using the PowerSoil DNA isolation kit (QIAGEN, Hilden, Germany) on the automated QIAcube platform using the inhibitory removal technology (IRT) protocol. The V4 hypervariable region of the 16S rRNA gene was amplified and sequenced using the 505F/816R primer set[59]. Paired-end sequencing was done at a length of 301 nucleotides (nt) on the Illumina MiSeq platform by the University of Minnesota Genomics Center using their previously described dual-index method[60]. Two negative controls (sterile water) were carried through the DNA extraction and sequencing process or amplification and sequencing alone. Neither produced quantifiable amplicons. Raw sequence data are deposited in the Sequence Read Archive under BioProject accession number SRP325945.

Fecal amplicon sequence processing and annotation

Sequence data processing and analysis were done using mothur ver. 1.41.1[61]. Forward and reverse reads were trimmed to 170 nt and paired-end joined using fastq join software.[4] Joined reads were quality trimmed over a sliding window of 50 nt and an average score of 35. Sequences with ambiguous bases, >8 nt homopolymers, or >2 nt mismatches to primer sequences were removed. High-quality sequences were subjected to a 2% pre-clustering step[62] and chimeras were identified and removed using UCHIME ver. 4.2.40[63]. Sequences were aligned against the SILVA database[64] (ver. 138) for processing. Clustering of operational taxonomic units was done at 99% similarity using the furthest-neighbor algorithm and taxonomic classifications were made against the Ribosomal Database Project (ver. 18)[65]. Compositional data are reported from non-normalized data. For statistical comparisons, samples were rarefied to 10,000 reads/sample[66].

Fecal statistical analysis

Alpha diversity was calculated as the Shannon and Chao1 indices. Beta diversity was evaluated using Bray-Curtis dissimilarity matrices[67]. Ordination of samples was done using principal coordinate analysis[68], and differences in community composition were evaluated by analysis of similarity (ANOSIM), with Bonferroni correction for multiple comparisons[69]. Differences in alpha diversity were determined by ANOVA with Tukey's posthoc test and differences in genera relative abundances were evaluated by the non-parametric Kruskal-Wallis test, with pairwise comparisons done using the Steel-Dwass-Critchlow-Fligner procedure. To determine dissimilarity from baseline composition, SourceTracker2[70] was used with baseline samples in each group designated as the source. All statistics were evaluated at α=0.05 prior to correction for multiple comparisons.

Spatial sequencing

Fixed moused liver sections were mounted and stained with DAPI and an anti-CD68 to create macrophage-free ROIs. Fixed human liver sections were mounted and stained with DAPI and anti-CD68 and anti-panCK antibodies to create zone-specific ROIs. Spatial sequencing was performed as previously described using the GeoMx platform (NanoString)[71]. Analysis of the sequencing data was performed on the GeoMx Digital Spatial Profiler (NanoString).

Single-cell RNA sequencing

Cells from each sample were individually incubated with cell multiplexing oligos (CMO) to allow for downstream multiplexing of samples. Following, samples were combined and loaded into capture ports of a 10x-Genomics chip following a single cell 3' kit. Separate libraries were created for gene expression and CMO and sequenced utilizing a Novaseq S4 chip (2 x 150bp PE). Feature quantification was performed using cellranger (version 3.0, 10X Genomics). All subsequent analyses were performed using Seurat 3.1.1[72]. After sample demultiplexing of CMOs, we retained single cells and normalized within each pool using the 4 sctransform method in Seurat[72]. Visualization of different clusters was enabled using Uniform Manifold Approximation and Projection (UMAP) dimensional reduction[73]. The Seurat cell ID function was utilized to identify monocytes and macrophages, which were re-clustered for analysis. Differential expression testing was performed using the default Wilcoxon rank-sum test.

Statistical Analysis

Statistical significance was determined using a one-way ANOVA with Holm-Šídák multiple comparison test using GraphPad Prism 8.3. All data analyzed by ANOVA followed a Gaussian distribution (Shapiro-Wilk test) and had equal variances (Brown-Forsythe). For datasets that failed the normality test, statistical significance was determined using multiple non-parametric Mann-Whitney tests. Mouse studies were repeated in at least two independent experiments. Data are presented as means ± SEM with statistical significance denoted.

REFERENCES

1. Younossi, Z., et al., *Global burden of NAFLD and NASH: trends, predictions, risk factors and prevention.* Nat Rev Gastroenterol Hepatol, 2018. **15**(1): p. 11-20.
2. Marengo, A., R.I. Jouness, and E. Bugianesi, *Progression and Natural History of Nonalcoholic Fatty Liver Disease in Adults.* Clin Liver Dis, 2016. **20**(2): p. 313-24.
3. Tilg, H. and A.R. Moschen, *Evolution of inflammation in nonalcoholic fatty liver disease: the multiple parallel hits hypothesis.* Hepatology, 2010. **52**(5): p. 1836-46.
4. Schuster, S., et al., *Triggering and resolution of inflammation in NASH.* Nat Rev Gastroenterol Hepatol, 2018. **15**(6): p. 349-364.
5. Yanovski, S.Z. and J.A. Yanovski, *Obesity.* N Engl J Med, 2002. **346**(8): p. 591-602.
6. Stefater, M.A., et al., *All bariatric surgeries are not created equal: insights from mechanistic comparisons.* Endocr Rev, 2012. **33**(4): p. 595-622.
7. Inge, T.H., et al., *Perioperative outcomes of adolescents undergoing bariatric surgery: the Teen-Longitudinal Assessment of Bariatric Surgery (Teen-LABS) study.* JAMA Pediatr, 2014. **168**(1): p. 47-53.
8. Cherla, D.V., et al., *Impact of sleeve gastrectomy and Roux-en-Y gastric bypass on biopsy-proven non-alcoholic fatty liver disease.* Surg Endosc, 2020. **34**(5): p. 2266-2272.
9. Froylich, D., et al., *Effect of Roux-en-Y gastric bypass and sleeve gastrectomy on nonalcoholic fatty liver disease: a comparative study.* Surg Obes Relat Dis, 2016. **12**(1): p. 127-31.
10. Wickremesekera, K., et al., *Loss of insulin resistance after Roux-en-Y gastric bypass surgery: a time course study.* Obes Surg, 2005. **15**(4): p. 474-81.
11. Rizzello, M., et al., *Early postoperative insulin-resistance changes after sleeve gastrectomy.* Obes Surg, 2010. **20**(1): p. 50-5.
12. Ryan, K.K., et al., *FXR is a molecular target for the effects of vertical sleeve gastrectomy.* Nature, 2014. **509**(7499): p. 183-8.
13. le Roux, C.W., et al., *Gut hormones as mediators of appetite and weight loss after Roux-en-Y gastric bypass.* Ann Surg, 2007. **246**(5): p. 780-5.
14. Saeidi, N., et al., *Reprogramming of intestinal glucose metabolism and glycemic control in rats after gastric bypass.* Science, 2013. **341**(6144): p. 406-10.
15. Jahansouz, C., et al., *Sleeve gastrectomy drives persistent shifts in the gut microbiome.* Surg Obes Relat Dis, 2017. **13**(6): p. 916-924.
16. Liou, A.P., et al., *Conserved shifts in the gut microbiota due to gastric bypass reduce host weight and adiposity.* Sci Transl Med, 2013. **5**(178): p. 178ra41.
17. Remmerie, A., et al., *Osteopontin Expression Identifies a Subset of Recruited Macrophages Distinct from Kupffer Cells in the Fatty Liver.* Immunity, 2020. **53**(3): p. 641-657 e14.
18. Xiong, X., et al., *Landscape of Intercellular Crosstalk in Healthy and NASH Liver Revealed by Single-Cell Secretome Gene Analysis.* Mol Cell, 2019. **75**(3): p. 644-660 e5.
19. Guilliams, M., et al., *Spatial proteogenomics reveals distinct and evolutionarily conserved hepatic macrophage niches.* Cell, 2022. **185**(2): p. 379-396.e38.
20. Hendrikx, T., et al., *Soluble TREM2 levels reflect the recruitment and expansion of TREM2(+) macrophages that localize to fibrotic areas and limit NASH.* J Hepatol, 2022.
21. Hou, J., et al., *TREM2 sustains macrophage-hepatocyte metabolic coordination in nonalcoholic fatty liver disease and sepsis.* J Clin Invest, 2021. **131**(4): p. e135197.
22. Wang, X., et al., *Prolonged hypernutrition impairs TREM2-dependent efferocytosis to license chronic liver inflammation and NASH development.* Immunity, 2023. **56**(1): p. 58-77.e11.
23. Perugorria, M.J., et al., *Non-parenchymal TREM-2 protects the liver from immune-mediated hepatocellular damage.* Gut, 2019. **68**(3): p. 533-546.

24. Deczkowska, A., A. Weiner, and I. Amit, *The Physiology, Pathology, and Potential Therapeutic Applications of the TREM2 Signaling Pathway.* Cell, 2020. **181**(6): p. 1207-1217.
25. Jaitin, D.A., et al., *Lipid-Associated Macrophages Control Metabolic Homeostasis in a Trem2-Dependent Manner.* Cell, 2019. **178**(3): p. 686-698 e14.
26. Asgharpour, A., et al., *A diet-induced animal model of non-alcoholic fatty liver disease and hepatocellular cancer.* J Hepatol, 2016. **65**(3): p. 579-88.
27. Ben-Zvi, D., et al., *Time-Dependent Molecular Responses Differ between Gastric Bypass and Dieting but Are Conserved Across Species.* Cell Metab, 2018. **28**(2): p. 310-323 e6.
28. Ghazarian, M., et al., *Type I Interferon Responses Drive Intrahepatic T cells to Promote Metabolic Syndrome.* Sci Immunol, 2017. **2**(10).
29. Daemen, S., et al., *Dynamic Shifts in the Composition of Resident and Recruited Macrophages Influence Tissue Remodeling in NASH.* Cell Reports, 2021. **34**(2): p. 108626.
30. Street, K., et al., *Slingshot: cell lineage and pseudotime inference for single-cell transcriptomics.* BMC Genomics, 2018. **19**(1): p. 477.
31. Hendrikx, T., et al., *Soluble TREM2 levels reflect the recruitment and expansion of TREM2(+) macrophages that localize to fibrotic areas and limit NASH.* J Hepatol, 2022. **77**(5): p. 1373-1385.
32. Lassailly, G., et al., *Bariatric Surgery Provides Long-term Resolution of Nonalcoholic Steatohepatitis and Regression of Fibrosis.* Gastroenterology, 2020. **159**(4): p. 1290-1301.e5.
33. le Roux, C.W. and M. Bueter, *The physiology of altered eating behaviour after Roux-en-Y gastric bypass.* Exp Physiol, 2014. **99**(9): p. 1128-32.
34. Arble, D.M., et al., *Metabolic comparison of one-anastomosis gastric bypass, single-anastomosis duodenal-switch, Roux-en-Y gastric bypass, and vertical sleeve gastrectomy in rat.* Surg Obes Relat Dis, 2018. **14**(12): p. 1857-1867.
35. Hofso, D., et al., *Beta cell function after weight loss: a clinical trial comparing gastric bypass surgery and intensive lifestyle intervention.* Eur J Endocrinol, 2011. **164**(2): p. 231-8.
36. Ding, L., et al., *Vertical sleeve gastrectomy confers metabolic improvements by reducing intestinal bile acids and lipid absorption in mice.* Proceedings of the National Academy of Sciences, 2021. **118**(6): p. e2019388118.
37. Biobaku, F., et al., *Bariatric Surgery: Remission of Inflammation, Cardiometabolic Benefits, and Common Adverse Effects.* J Endocr Soc, 2020. **4**(9): p. bvaa049.
38. Ahn, C.H., et al., *Vertical sleeve gastrectomy induces distinctive transcriptomic responses in liver, fat and muscle.* Sci Rep, 2021. **11**(1): p. 2310.
39. Griffin, C., et al., *Inflammatory responses to dietary and surgical weight loss in male and female mice.* Biology of Sex Differences, 2019. **10**(1): p. 16.
40. Han, H., et al., *Macrophage-derived Osteopontin (SPP1) Protects From Nonalcoholic Steatohepatitis.* Gastroenterology, 2023.
41. Furet, J.P., et al., *Differential adaptation of human gut microbiota to bariatric surgery-induced weight loss: links with metabolic and low-grade inflammation markers.* Diabetes, 2010. **59**(12): p. 3049-57.
42. Kong, L.C., et al., *Gut microbiota after gastric bypass in human obesity: increased richness and associations of bacterial genera with adipose tissue genes.* Am J Clin Nutr, 2013. **98**(1): p. 16-24.
43. Cani, P.D., et al., *Changes in gut microbiota control metabolic endotoxemia-induced inflammation in high-fat diet-induced obesity and diabetes in mice.* Diabetes, 2008. **57**(6): p. 1470-81.

44. Caesar, R., et al., *Crosstalk between Gut Microbiota and Dietary Lipids Aggravates WAT Inflammation through TLR Signaling.* Cell Metab, 2015. **22**(4): p. 658-68.
45. Shao, Y., et al., *Vertical sleeve gastrectomy increases duodenal Lactobacillus spp. richness associated with the activation of intestinal HIF2α signaling and metabolic benefits.* Mol Metab, 2022. **57**: p. 101432.
46. Daws, M.R., et al., *Pattern Recognition by TREM-2: Binding of Anionic Ligands.* The Journal of Immunology, 2003. **171**(2): p. 594-599.
47. Weaver, L.K., et al., *Microbiota-dependent signals are required to sustain TLR-mediated immune responses.* JCI Insight, 2019. **4**(1).
48. Abu-Gazala, S., et al., *Sleeve Gastrectomy Improves Glycemia Independent of Weight Loss by Restoring Hepatic Insulin Sensitivity.* Diabetes, 2018. **67**(6): p. 1079-1085.
49. Wu, Y., et al., *TREM-2 is a sensor and activator of T cell response in SARS-CoV-2 infection.* Sci Adv, 2021. **7**(50): p. eabi6802.
50. Wu, Y., et al., *TREM-2 promotes Th1 responses by interacting with the CD3ζ-ZAP70 complex following Mycobacterium tuberculosis infection.* The Journal of Clinical Investigation, 2021. **131**(17).
51. Jaitin, D.A., et al., *Lipid-Associated Macrophages Control Metabolic Homeostasis in a Trem2-Dependent Manner.* Cell, 2019. **178**(3): p. 686-698.e14.
52. Lynch, R.W., et al., *An efficient method to isolate Kupffer cells eliminating endothelial cell contamination and selective bias.* J Leukoc Biol, 2018. **104**(3): p. 579-586.
53. Bailey, J.D., et al., *Isolation and culture of murine bone marrow-derived macrophages for nitric oxide and redox biology.* Nitric Oxide, 2020. **100-101**: p. 17-29.
54. Kraus, D., Q. Yang, and B.B. Kahn, *Lipid Extraction from Mouse Feces.* Bio Protoc, 2015. **5**(1).
55. Troyanskaya, O., et al., *Missing value estimation methods for DNA microarrays.* Bioinformatics, 2001. **17**(6): p. 520-525.
56. Mohamed, A. and M.M. Hill, *LipidSuite: interactive web server for lipidomics differential and enrichment analysis.* Nucleic Acids Research, 2021. **49**(W1): p. W346-W351.
57. Krautbauer, S. and G. Liebisch, *LC-MS/MS Analysis of Bile Acids*, in *Clinical Metabolomics: Methods and Protocols*, M. Giera, Editor. 2018, Springer New York: New York, NY. p. 103-110.
58. Ge, S.X., E.W. Son, and R. Yao, *iDEP: an integrated web application for differential expression and pathway analysis of RNA-Seq data.* BMC Bioinformatics, 2018. **19**(1): p. 534.
59. Caporaso, J.G., et al., *Ultra-high-throughput microbial community analysis on the Illumina HiSeq and MiSeq platforms.* The ISME Journal, 2012. **6**(8): p. 1621-1624.
60. Gohl, D.M., et al., *Systematic improvement of amplicon marker gene methods for increased accuracy in microbiome studies.* Nature Biotechnology, 2016. **34**(9): p. 942-949.
61. Schloss Patrick, D., et al., *Introducing mothur: Open-Source, Platform-Independent, Community-Supported Software for Describing and Comparing Microbial Communities.* Applied and Environmental Microbiology, 2009. **75**(23): p. 7537-7541.
62. Huse, S.M., et al., *Ironing out the wrinkles in the rare biosphere through improved OTU clustering.* Environ Microbiol, 2010. **12**(7): p. 1889-98.
63. Edgar, R.C., et al., *UCHIME improves sensitivity and speed of chimera detection.* Bioinformatics, 2011. **27**(16): p. 2194-2200.
64. Pruesse, E., et al., *SILVA: a comprehensive online resource for quality checked and aligned ribosomal RNA sequence data compatible with ARB.* Nucleic Acids Res, 2007. **35**(21): p. 7188-96.
65. Cole, J.R., et al., *The Ribosomal Database Project: improved alignments and new tools for rRNA analysis.* Nucleic Acids Research, 2009. **37**(suppl_1): p. D141-D145.

66. Gihring, T.M., S.J. Green, and C.W. Schadt, *Massively parallel rRNA gene sequencing exacerbates the potential for biased community diversity comparisons due to variable library sizes.* Environ Microbiol, 2012. **14**(2): p. 285-90.
67. Bray, J.R. and J.T. Curtis, *An Ordination of the Upland Forest Communities of Southern Wisconsin.* Ecological Monographs, 1957. **27**(4): p. 325-349.
68. Anderson, M.J. and T.J. Willis, *CANONICAL ANALYSIS OF PRINCIPAL COORDINATES: A USEFUL METHOD OF CONSTRAINED ORDINATION FOR ECOLOGY.* Ecology, 2003. **84**(2): p. 511-525.
69. Clarke, K.R., *Non-parametric multivariate analyses of changes in community structure.* Australian Journal of Ecology, 1993. **18**(1): p. 117-143.
70. Knights, D., et al., *Bayesian community-wide culture-independent microbial source tracking.* Nature Methods, 2011. **8**(9): p. 761-763.
71. Zollinger, D.R., et al., *GeoMx™ RNA Assay: High Multiplex, Digital, Spatial Analysis of RNA in FFPE Tissue*, in *In Situ Hybridization Protocols*, B.S. Nielsen and J. Jones, Editors. 2020, Springer US: New York, NY. p. 331-345.
72. Hafemeister, C. and R. Satija, *Normalization and variance stabilization of single-cell RNA-seq data using regularized negative binomial regression.* Genome Biology, 2019. **20**(1): p. 296.
73. Becht, E., et al., *Dimensionality reduction for visualizing single-cell data using UMAP.* Nature Biotechnology, 2019. **37**(1): p. 38-44.

FIGURE LEGENDS

Figure 1. Vertical sleeve gastrectomy ameliorates NASH progression independent of weight-loss

(A-O) Mice were fed an HFHC diet for 12 weeks and then for 5 weeks post-surgery.
(A) Experimental design.
(B) Mean daily food intake post-surgery; Sham AL (n = 17), Sham PF (n = 17), VSG (n = 19).
(C) Weekly body weights post-surgery; Sham AL (n = 17), Sham PF (n = 17), VSG (n = 26).
(D) Final liver weight; NCD (n = 25), Sham AL (n = 17), Sham PF (n = 17), VSG (n = 25).
(E) Hepatic triglyceride content; NCD (n = 11), Sham AL (n = 12), Sham PF (n = 16), VSG (n = 21).
(F) Representative H&E-stained liver sections.
(G) NAS score; NCD (n = 8), Sham AL (n = 6), Sham PF (n = 4), VSG (n = 5).
(H) Serum ALT (Left), Serum AST (Right); NCD (n = 25), Sham AL (n = 17), Sham PF (n = 17), VSG (n = 25).
(I) Fecal lipid content; Sham AL (n = 6), Sham PF (n = 6), VSG (n = 6).
(J) Relative abundance of microbiota species; NCD (n = 5-12), Sham AL (n = 6), Sham PF (n = 10), VSG (n = 13).
(K) Abundance of Clostridium XVIII; NCD (n = 5-12), Sham AL (n = 6), Sham PF (n = 10), VSG (n = 13).
(L) Abundance of Lactobacillus; NCD (n = 5-12), Sham AL (n = 6), Sham PF (n = 10), VSG (n = 13).
(M) Total portal vein bile acids; NCD (n = 10), Sham AL (n = 6), Sham PF (n = 8), VSG (n = 12)
(N) Concentration of portal vein TCA, DCA, and TDCA; NCD (n = 10), Sham AL (n = 6), Sham PF (n = 8), VSG (n = 12).
(O) Total portal vein short chain fatty acids (SCFA); NCD (n = 10), Sham AL (n = 6), Sham PF (n = 8), VSG (n = 11).
Data are presented as mean ± SEM.

Figure 2. Single-cell RNA sequencing reveals that lipid-associated macrophages are responsive to bariatric surgery

(A) scRNA-seq of hepatic immune cells 5 and 10 weeks post-VSG.
(A) Experimental design.
(B) Uniform manifold approximation and projection (UMAP) analysis of all monocytes and macrophages and expression of marker genes.
(C) Heatmap of most highly expressed genes per cluster.
(D) Slingshot trajectory analysis (left) and gene expression over pseudotime for each trajectory (right).
(E) UMAP visualization of monocytes and macrophages for each group and time point (top) and relative proportion of each cluster (bottom).
(F) UMAP visualization of Trem2 expression.
All data presented in this figure (n = 4).

Figure 3. Bariatric surgery exerts anti-inflammatory effects on lipid-associated macrophages

Volcano plot of DEGs for VSG vs. Sham AL (left) and VSG vs. Sham PF (right).
All data presented in this figure (n = 4).

Figure 4. Spatial transcriptomic analysis of NASH livers following bariatric surgery
(A-I) Spatial sequencing of liver sections 5 weeks post-VSG
(A) Representative liver section used for GeoMx. Orange shading highlights $CD68^-$ regions of interest (ROI) and green/orange shading is CD68+ ROI.
(B) Experimental design for processing data (top) and the total number of genes after each processing stop (bottom).
(C) Unsupervised PCA of CD68+ and CD68- ROIs.
(D) Volcano plot of CD68- Lean vs. Sham AL.
(E) Volcano plot of CD68- Sham AL vs. VSG.
(F) Volcano plot of CD68- Sham PF vs. VSG.
(G) Pathway analysis for Lean vs. Sham AL (metabolism and immune pathways).
(H) Pathway analysis for Sham AL vs. VSG (metabolism and immune pathways).
(I) Pathway analysis for Sham PF vs. VSG (metabolism and immune pathways).
All data presented in this figure (n = 4).

Figure 5. LAMs mediate VSG-induced NASH reversal
(A-H) WT and Trem2 KO mice were fed an HFHC diet for 12 weeks and then for 5 weeks post-surgery.
(A) Percent change in bodyweight post-surgery; WT Sham (n = 8), WT VSG (n = 7), KO Sham (n = 8), KO VSG (n = 8).
(B) Fecal lipid content; WT Sham (n = 5), WT VSG (n = 6), KO Sham (n = 7), KO VSG (n = 8).
(C) Liver Weight; WT Sham (n = 8), WT VSG (n = 7), KO Sham (n = 8), KO VSG (n = 8).
(D) Representative H&E-stained liver sections.
(E) Hepatic triglyceride content; WT Sham (n = 8), WT VSG (n = 7), KO Sham (n = 8), KO VSG (n = 8).
(F) Serum ALT; WT Sham (n = 8), WT VSG (n = 7), KO Sham (n = 8), KO VSG (n = 8).
(G) Serum AST; WT Sham (n = 8), WT VSG (n = 7), KO Sham (n = 8), KO VSG (n = 8).
(H) Pathway analysis of WT VSG vs. KO VSG macrophages, GO biological process (top) and KEGG pathway (bottom).
(I) qPCR of inflammatory cytokines in bone marrow-derived macrophages (BMDM) stimulated with palmitate (PA); WT (n = 7), KO (n = 6, top) and unstimulated (unstim); WT (n = 3), KO (n = 4, bottom).
Data are presented as mean ± SEM.

Figure 6. Bariatric surgery alters the lipid profile in hepatic macrophages
(A-I) FIA-MS/MS and LC-MS/MS of VSG and Sham AL hepatic macrophages 5 weeks post-surgery.
(A) Frequency of detectable metabolites as a proportion of all detectable metabolites.
(B) Unsupervised PCA of VSG and Sham AL hepatic macrophage metabolites.
(C) Concentration of major lipid species in VSG and Sham AL macrophages.
(D) Concentration of phosphatidylcholine (PC) subspecies.
(E) Concentration of sphingolipid (SM) subspecies.
(F) Concentration of fatty acid (FA) subspecies.
(G) Concentration of cholesterol ester (CE) subspecies.
(H) Concentration of ceramide (Cer) subspecies.
(I) Chain length enrichment of all lipid species.
All data presented in this figure (n = 4). Data are presented as mean ± SEM.

SUPPLEMENTAL FIGURE LEGENDS

Supplemental Figure 1. (related to Figure 1)

(A-F) Mice were fed an HFHC diet for 12 weeks and then for 10 weeks post-surgery.
(A) Percentage change in body weight 10 weeks post-surgery; Sham AL (n = 7), Sham PF (n = 6), VSG (n = 9).
(B) Liver weight 10 weeks post-surgery; NCD (n = 8), Sham AL (n = 7), Sham PF (n = 6), VSG (n = 9).
(C) Serum AST; NCD (n = 8), Sham AL (n = 7), Sham PF (n = 6), VSG (n = 9).
(D) Serum ALT; NCD (n = 8), Sham AL (n = 7), Sham PF (n = 6), VSG (n = 9).
(E) Hepatic triglyceride content; NCD (n = 8), Sham AL (n = 6), Sham PF (n = 6), VSG (n = 9).
(F) Concentration of portal vein bile acids; NCD (n = 10), Sham AL (n = 6), Sham PF (n = 8), VSG (n = 12).
Data are presented as mean ± SEM.

Supplemental Figure 2. (related to Figure 2)
Gene expression over pseudotime for lineage 1 (left) and 2 (right).
All data presented in this figure (n = 4).

Supplemental Figure 3. (related to Figure 3)
Heat maps of top DEGs between groups at both time points.
All data presented in this figure (n = 4).

Supplemental Figure 4. (related to Figure 4)
(A-F) Spatial sequencing of human liver samples pre-VSG and post-VSG
(A) Representative human liver sections used for GeoMx.
(B) Representative human liver section used for GeoMx with liver zones indicated.
(C) Unsupervised PCA of all human liver ROIs (n = 1).
(D) Pathway analysis for Zone 1 PreVSG vs. Zone 1 PostVSG.
(E) Pathway analysis for Zone 2 PreVSG vs. Zone 2 PostVSG.
(F) Heatmap of lipid-associated macrophage (LAM) genes.
(G) Pathway coverage for mouse VSG analysis.

Supplemental Figure 5. (related to Figure 5)
(A-I) WT and Trem2 KO mice were fed an HFHC diet for 12 weeks.
(A) Experimental design.
(B) Bodyweight after 12 weeks of diet (BW).
(C) Representative flow cytometry plots.
(D) Total number of polymorphonuclear (PMN) cells.
(E) Total number of monocyte-derived macrophages (moKCs).
(F) Total number of polymorphonuclear cells.
(G) Total number of F4/80^{hi}, CD11b^{int} macrophages.
(H) Total number of embryonic Kupffer cells (emKC).
(I) Total number of monocyte derived Kupffer cells (moKC).
Data are presented as mean ± SEM.

Supplemental Figure 6. (related to Figure 5)
(A-F) RNA sequencing of WT and Trem2 KO hepatic macrophages 5 weeks post-surgery.
(A) Unsupervised PCA of sequenced hepatic macrophages.

(B) Venn diagram of differentially expressed genes (DEG) for the WT Sham vs WT VSG and KO Sham vs KO VSG comparisons.
(C) Heat map of the top 500 most variable genes between WT Sham and WT VSG.
(D) Heat map of the top 500 most variable genes between KO Sham and KO VSG.
(E) Pathway analysis of WT Sham vs. WT VSG macrophages, GO biological process (top) and KEGG pathway (bottom).
(F) Pathway analysis of KO Sham vs. KO VSG macrophages, GO biological process (top) and KEGG pathway (bottom).
All data presented in this figure (n = 4). Data are presented as mean ± SEM.

Figure 1

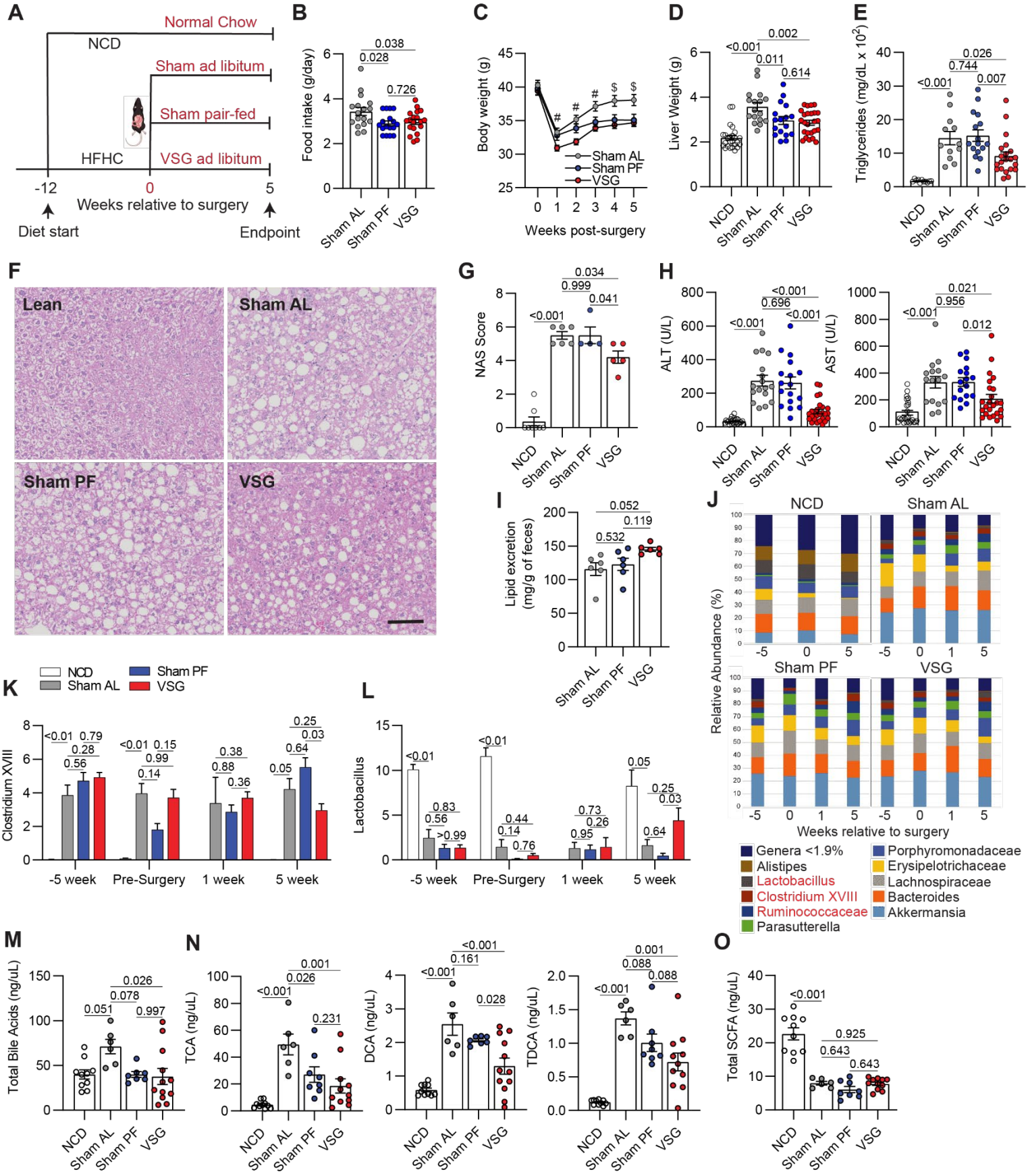
A
Normal Chow
NCD
Sham ad libitum
Sham pair-fed
HFHC
VSG ad libitum
-12
0
5
Weeks relative to surgery
Diet start
Endpoint
B
Food intake (g/day)
0.038
0.028
0.726
Sham AL
Sham PF
VSG
C
Body weight (g)
Sham AL
Sham PF
VSG
Weeks post-surgery
D
Liver Weight (g)
<0.001
0.002
0.011
0.614
NCD
Sham AL
Sham PF
VSG
E
Triglycerides (mg/dL x 10²)
0.026
0.744
<0.001
0.007
F
Lean
Sham AL
Sham PF
VSG
G
NAS Score
0.034
0.999
0.041
<0.001
H
ALT (U/L)
AST (U/L)
<0.001
0.696
<0.001
0.021
0.956
0.012
I
Lipid excretion (mg/g of feces)
0.052
0.119
0.532
J
NCD
Sham AL
Sham PF
VSG
Relative Abundance (%)
Weeks relative to surgery
Genera <1.9%
Alistipes
Lactobacillus
Clostridium XVIII
Ruminococcaceae
Parasutterella
Porphyromonadaceae
Erysipelotrichaceae
Lachnospiraceae
Bacteroides
Akkermansia
K
Clostridium XVIII
-5 week
Pre-Surgery
1 week
5 week
L
Lactobacillus
M
Total Bile Acids (ng/uL)
N
TCA (ng/uL)
DCA (ng/uL)
TDCA (ng/uL)
O
Total SCFA (ng/uL)

Figure 2.

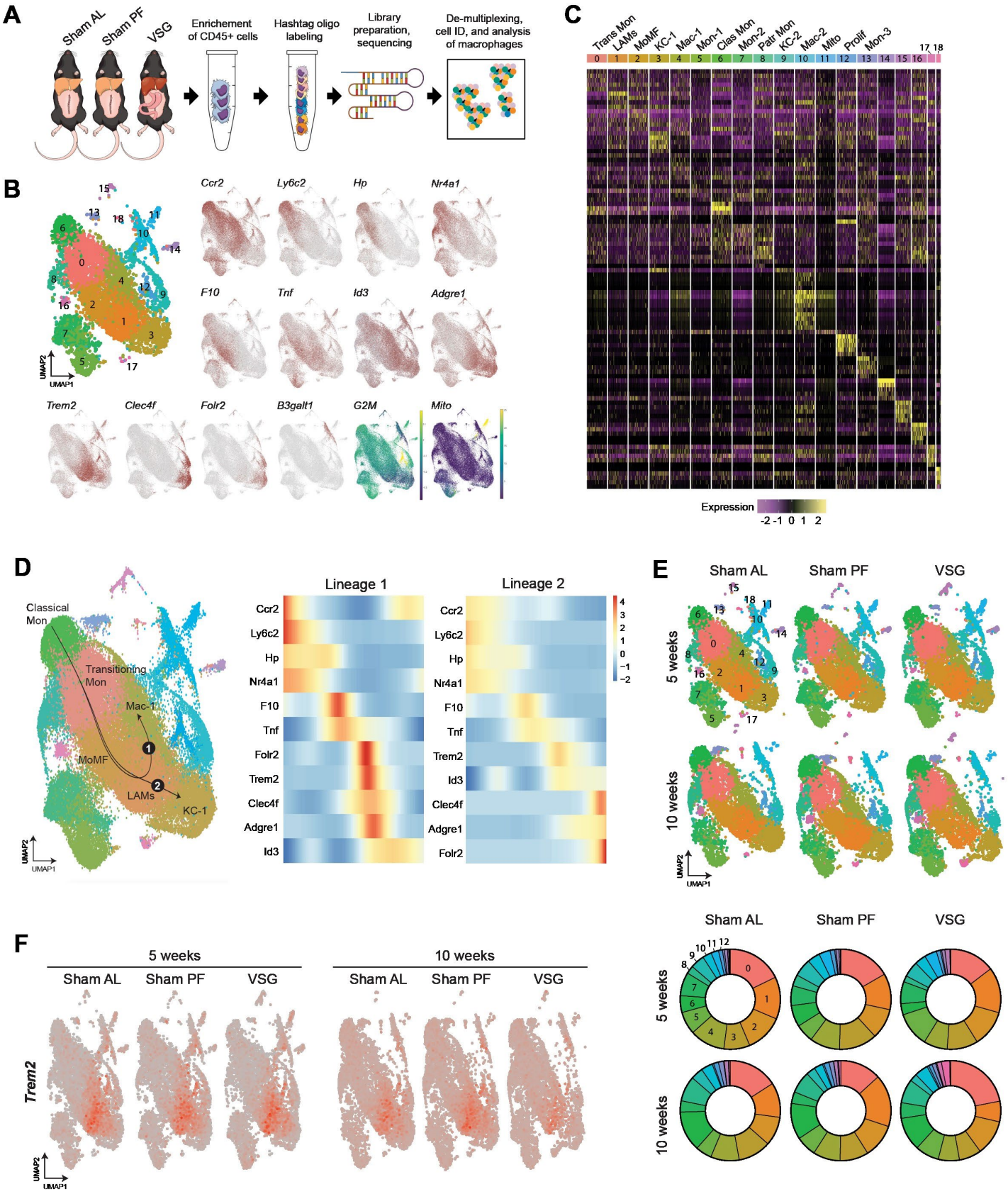
A
Sham AL
Sham PF
VSG
Enrichement of CD45+ cells
Hashtag oligo labeling
Library preparation, sequencing
De-multiplexing, cell ID, and analysis of macrophages
B
Ccr2
Ly6c2
Hp
Nr4a1
F10
Tnf
Id3
Adgre1
Trem2
Clec4f
Folr2
B3galt1
G2M
Mito
UMAP2
UMAP1
C
Trans Mon
LAMs
MoMF
KC-1
Mac-1
Mon-1
Clas Mon
Mon-2
Patr Mon
KC-2
Mac-2
Mito
Prolif
Mon-3
Expression
-2 -1 0 1 2
D
Classical Mon
Transitioning Mon
Mac-1
MoMF
LAMs
KC-1
Lineage 1
Lineage 2
Ccr2
Ly6c2
Hp
Nr4a1
F10
Tnf
Folr2
Trem2
Clec4f
Adgre1
Id3
E
Sham AL
Sham PF
VSG
5 weeks
10 weeks
F
5 weeks
10 weeks
Sham AL
Sham PF
VSG
Trem2

Figure 3.

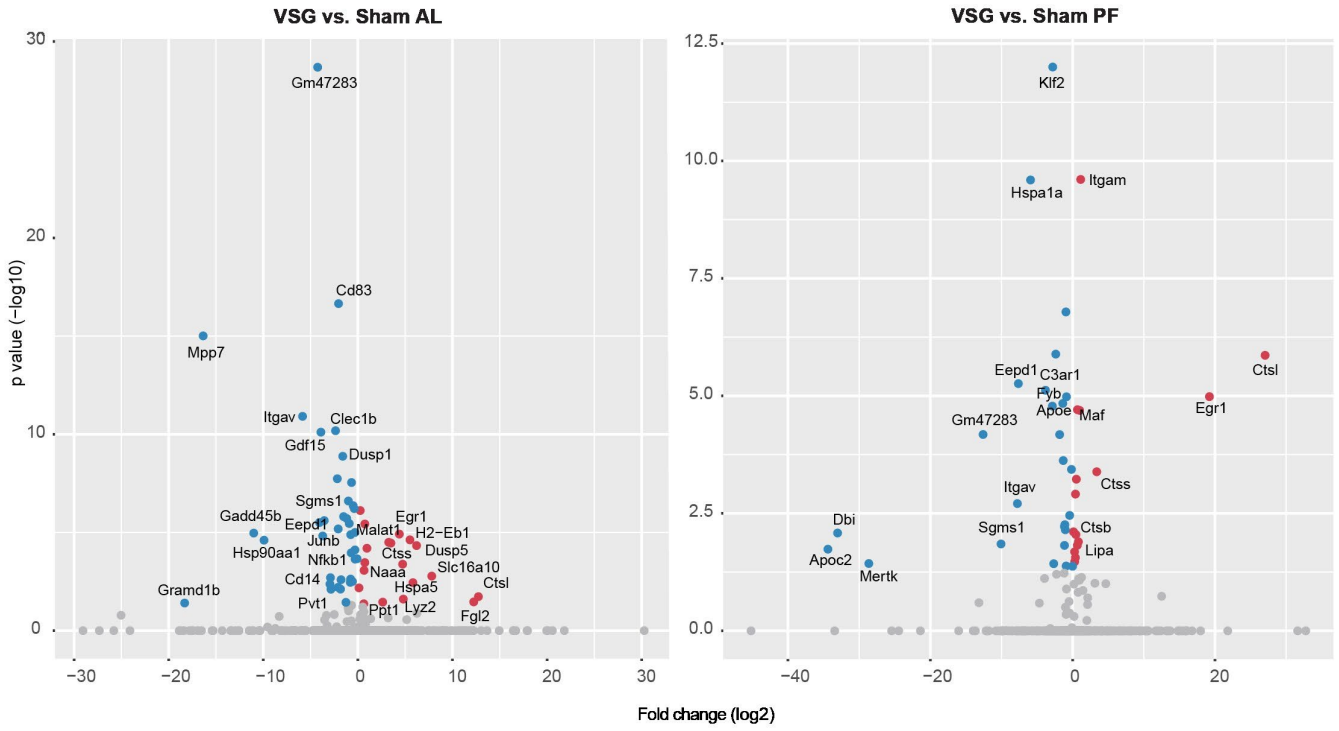
VSG vs. Sham AL
VSG vs. Sham PF
p value (−log10)
Fold change (log2)
Gm47283
Cd83
Mpp7
Itgav
Clec1b
Gdf15
Dusp1
Sgms1
Gadd45b
Eepd1
Egr1
Malat1
H2−Eb1
Junb
Hsp90aa1
Nfkb1
Ctss
Dusp5
Naaa
Slc16a10
Cd14
Hspa5
Ctsl
Gramd1b
Pvt1
Ppt1
Lyz2
Fgl2
Klf2
Hspa1a
Itgam
Eepd1
C3ar1
Fyb
Apoe
Maf
Ctsl
Egr1
Gm47283
Ctss
Itgav
Dbi
Sgms1
Ctsb
Lipa
Apoc2
Mertk

Figure 4.

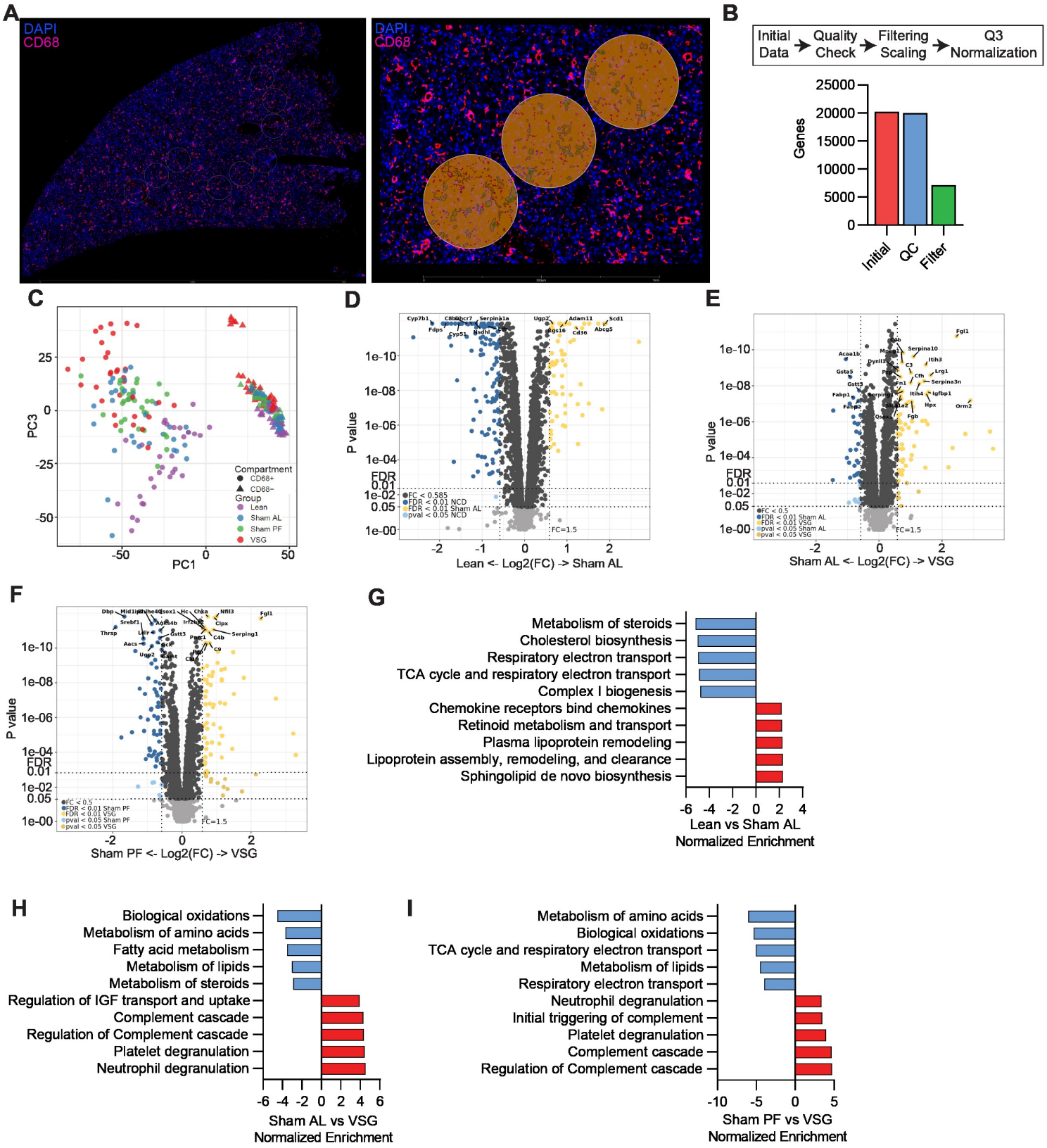
A
DAPI
CD68
B
Initial Data
Quality Check
Filtering Scaling
Q3 Normalization
Genes
25000
20000
15000
10000
5000
0
Initial
QC
Filter
C
PC3
PC1
Compartment
CD68+
CD68−
Group
Lean
Sham AL
Sham PF
VSG
D
P value
FDR
FC < 0.585
FDR < 0.01 NCD
FDR < 0.01 Sham AL
pval < 0.05 NCD
FC=1.5
Lean <- Log2(FC) -> Sham AL
E
P value
FDR
FC < 0.5
FDR < 0.01 Sham AL
FDR < 0.01 VSG
pval < 0.05 Sham AL
pval < 0.05 VSG
FC=1.5
Sham AL <- Log2(FC) -> VSG
F
P value
FDR
FC < 0.5
FDR < 0.01 Sham PF
FDR < 0.01 VSG
pval < 0.05 Sham PF
pval < 0.05 VSG
FC=1.5
Sham PF <- Log2(FC) -> VSG
G
Metabolism of steroids
Cholesterol biosynthesis
Respiratory electron transport
TCA cycle and respiratory electron transport
Complex I biogenesis
Chemokine receptors bind chemokines
Retinoid metabolism and transport
Plasma lipoprotein remodeling
Lipoprotein assembly, remodeling, and clearance
Sphingolipid de novo biosynthesis
Lean vs Sham AL
Normalized Enrichment
H
Biological oxidations
Metabolism of amino acids
Fatty acid metabolism
Metabolism of lipids
Metabolism of steroids
Regulation of IGF transport and uptake
Complement cascade
Regulation of Complement cascade
Platelet degranulation
Neutrophil degranulation
Sham AL vs VSG
Normalized Enrichment
I
Metabolism of amino acids
Biological oxidations
TCA cycle and respiratory electron transport
Metabolism of lipids
Respiratory electron transport
Neutrophil degranulation
Initial triggering of complement
Platelet degranulation
Complement cascade
Regulation of Complement cascade
Sham PF vs VSG
Normalized Enrichment

Figure 5.

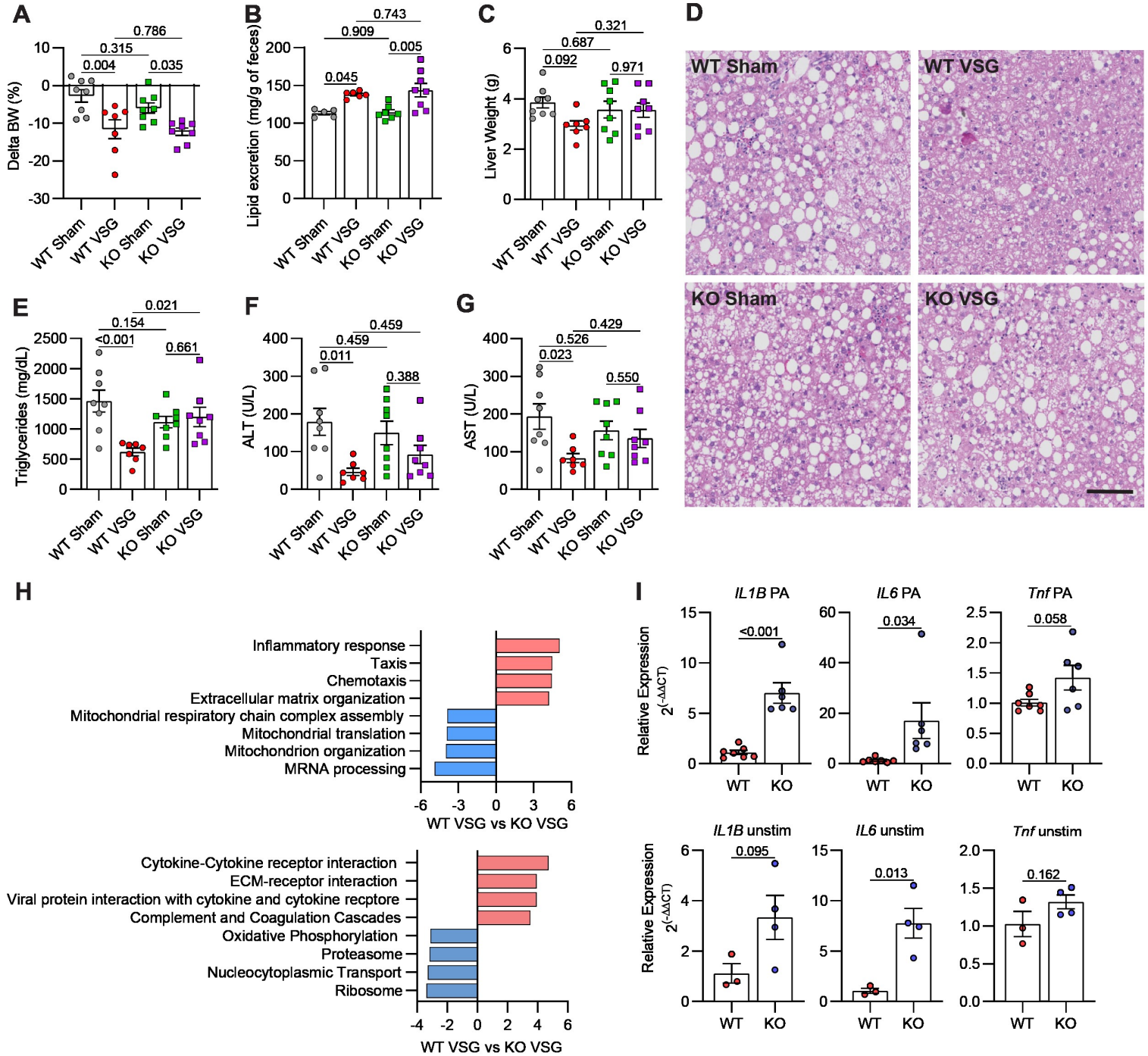
A
Delta BW (%)
0.004
0.315
0.786
0.035
WT Sham
WT VSG
KO Sham
KO VSG
B
Lipid excretion (mg/g of feces)
0.045
0.909
0.743
0.005
C
Liver Weight (g)
0.092
0.687
0.321
0.971
D
WT Sham
WT VSG
KO Sham
KO VSG
E
Triglycerides (mg/dL)
<0.001
0.154
0.021
0.661
F
ALT (U/L)
0.011
0.459
0.459
0.388
G
AST (U/L)
0.023
0.526
0.429
0.550
H
Inflammatory response
Taxis
Chemotaxis
Extracellular matrix organization
Mitochondrial respiratory chain complex assembly
Mitochondrial translation
Mitochondrion organization
MRNA processing
WT VSG vs KO VSG
Cytokine-Cytokine receptor interaction
ECM-receptor interaction
Viral protein interaction with cytokine and cytokine recptore
Complement and Coagulation Cascades
Oxidative Phosphorylation
Proteasome
Nucleocytoplasmic Transport
Ribosome
WT VSG vs KO VSG
I
IL1B PA
<0.001
IL6 PA
0.034
Tnf PA
0.058
IL1B unstim
0.095
IL6 unstim
0.013
Tnf unstim
0.162
Relative Expression
2(-ΔΔCT)
WT
KO

Figure 6.

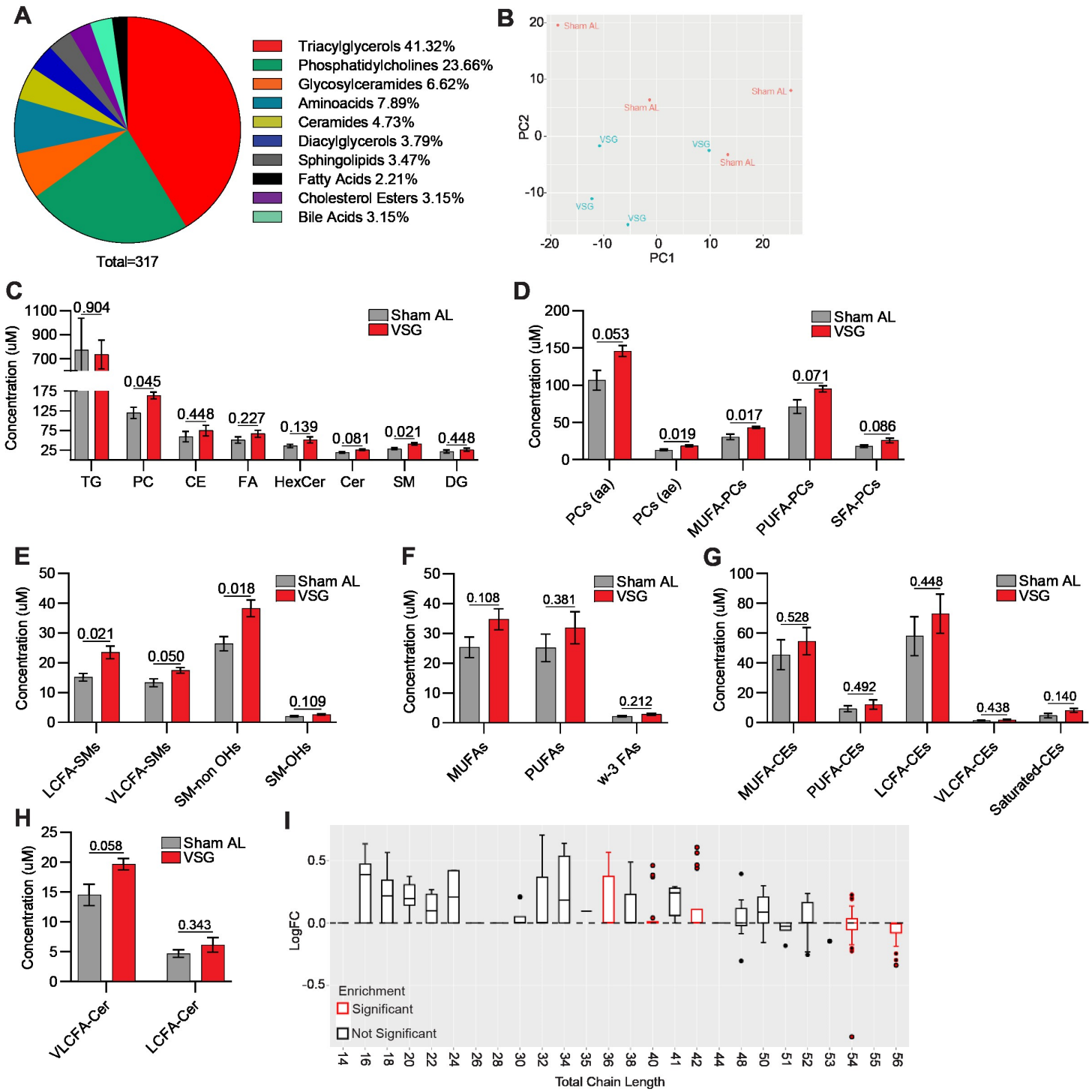
A
Triacylglycerols 41.32%
Phosphatidylcholines 23.66%
Glycosylceramides 6.62%
Aminoacids 7.89%
Ceramides 4.73%
Diacylglycerols 3.79%
Sphingolipids 3.47%
Fatty Acids 2.21%
Cholesterol Esters 3.15%
Bile Acids 3.15%
Total=317
B
Sham AL
VSG
PC1
PC2
C
Concentration (uM)
Sham AL
VSG
0.904
0.045
0.448
0.227
0.139
0.081
0.021
0.448
TG
PC
CE
FA
HexCer
Cer
SM
DG
D
Concentration (uM)
Sham AL
VSG
0.053
0.019
0.017
0.071
0.086
PCs (aa)
PCs (ae)
MUFA-PCs
PUFA-PCs
SFA-PCs
E
Concentration (uM)
Sham AL
VSG
0.021
0.050
0.018
0.109
LCFA-SMs
VLCFA-SMs
SM-non OHs
SM-OHs
F
Concentration (uM)
Sham AL
VSG
0.108
0.381
0.212
MUFAs
PUFAs
w-3 FAs
G
Concentration (uM)
Sham AL
VSG
0.528
0.492
0.448
0.438
0.140
MUFA-CEs
PUFA-CEs
LCFA-CEs
VLCFA-CEs
Saturated-CEs
H
Concentration (uM)
Sham AL
VSG
0.058
0.343
VLCFA-Cer
LCFA-Cer
I
LogFC
Enrichment
Significant
Not Significant
Total Chain Length

Supplemental Figure 1 (Related to Figure 1)

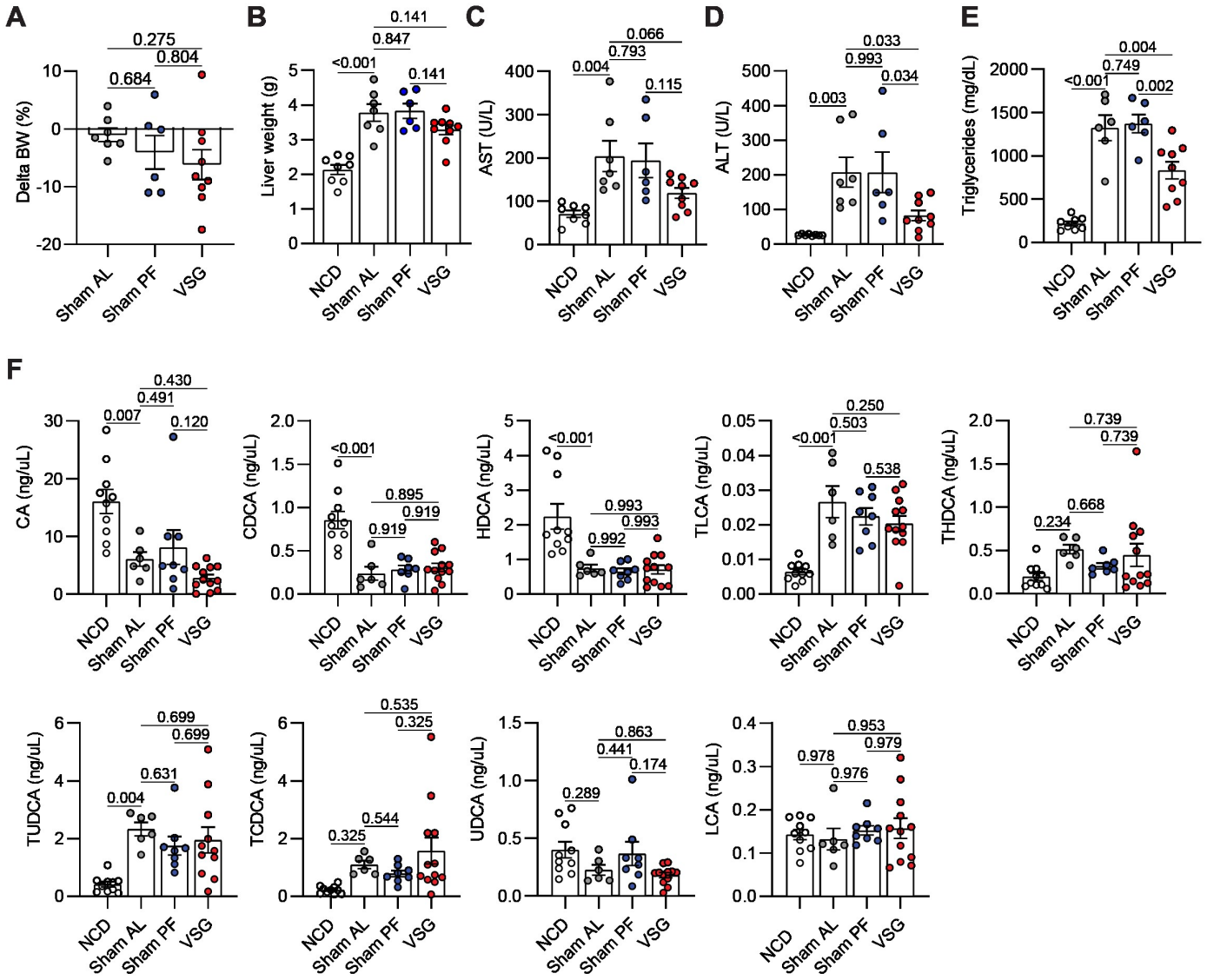

Supplemental Figure 2 (Related to Figure 2)

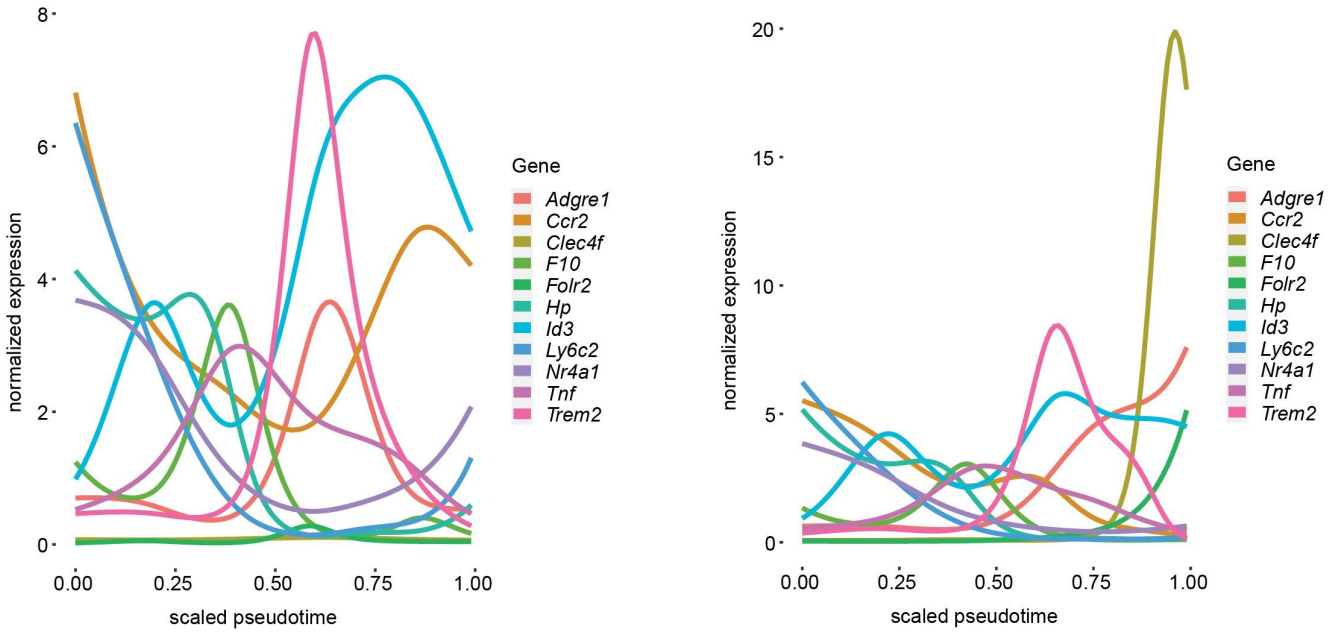

Supplemental Figure 3 (Related to Figure 3)

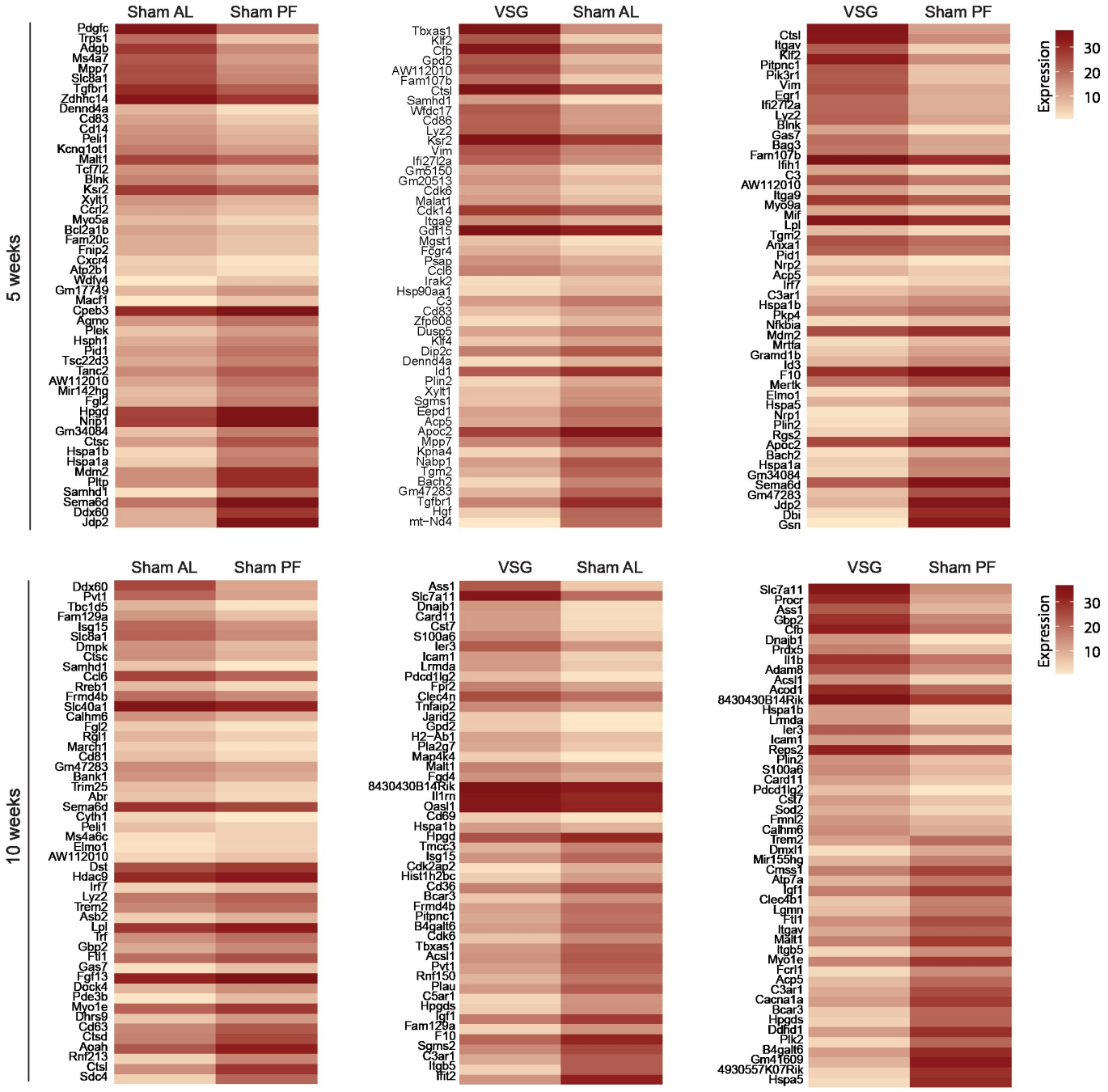

Supplemental Figure 4 (Related to Figure 4)

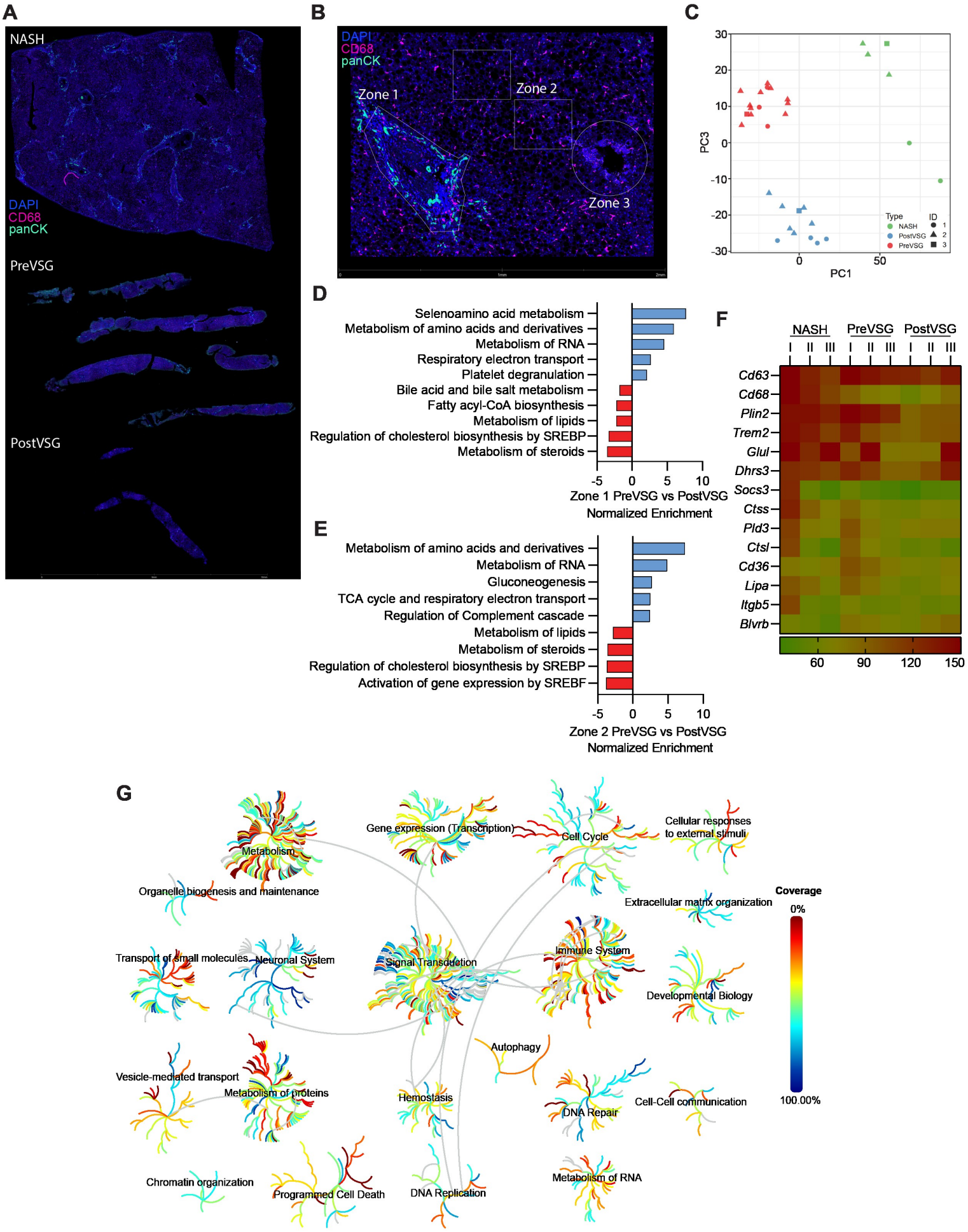

Supplemental Figure 5 (Related to Figure 5)

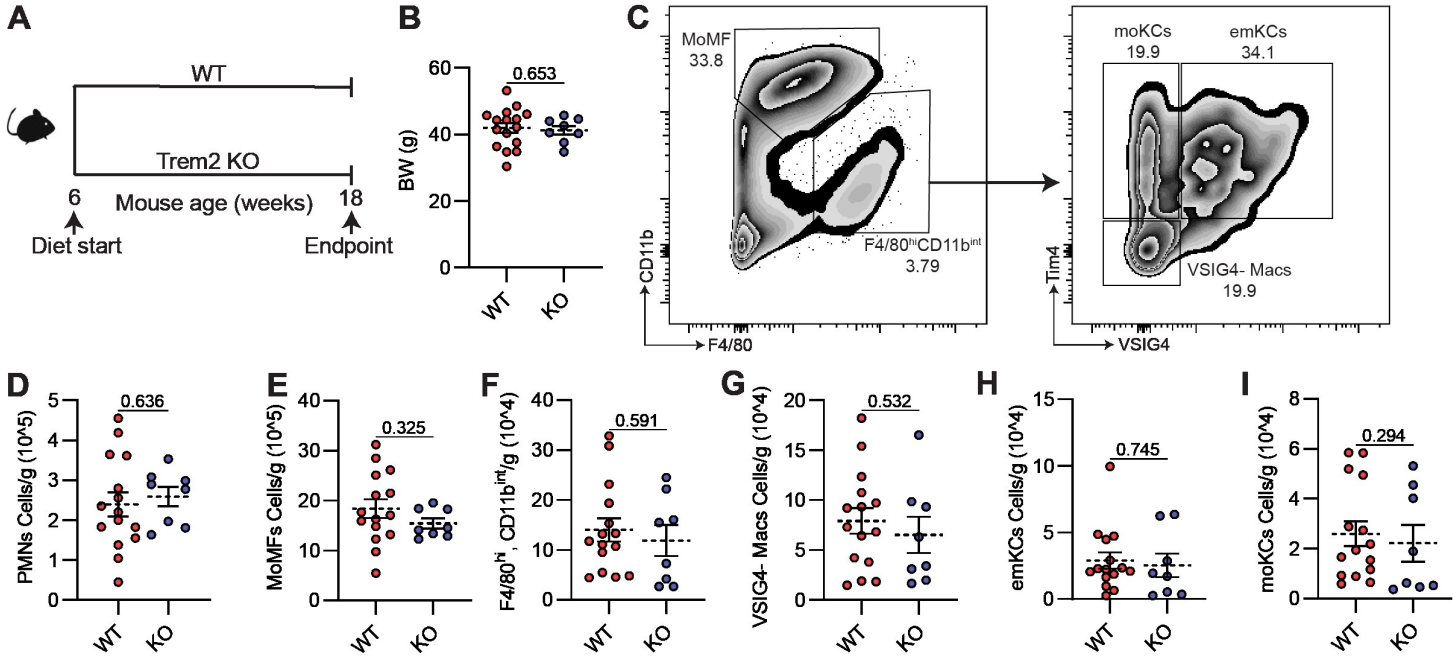
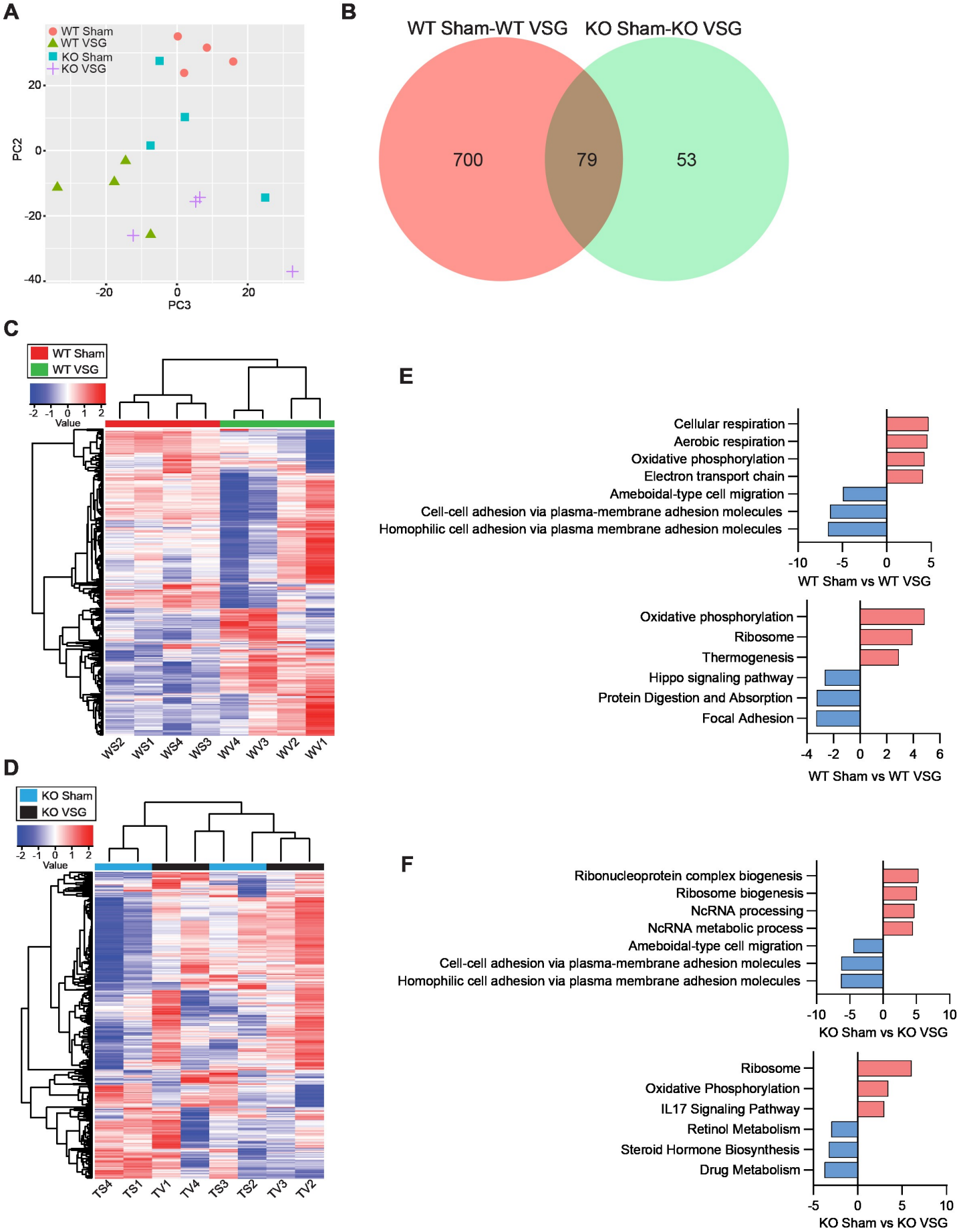
Supplemental Figure 6 (Related to Figure 5)